

# Perspective of high-speed Mach-Zehnder modulators based on nonlinear optics and complex band structures

Shuyi Li,<sup>1,\*</sup> Wei Luo,<sup>2,\*</sup> Zhenyu Li,<sup>3,†</sup> and Junqiu Liu<sup>1,4,‡</sup>

<sup>1</sup>*International Quantum Academy, Shenzhen 518048, China*

<sup>2</sup>*Department of Electrical and Electronic Engineering,*

*The Hong Kong Polytechnic University, Hong Kong, China*

<sup>3</sup>*Linkstar Microtronics Pte. Ltd., Singapore 118222, Singapore*

<sup>4</sup>*Hefei National Laboratory, University of Science and Technology of China, Hefei 230088, China*

(Dated: February 21, 2025)

Optical modulators are essential building blocks for high-capacity optical communication and massively parallel computing. Among all types of optical modulators, travelling-wave Mach-Zehnder modulators (TW-MZMs) featuring high speed and efficiency are widely used, and have been developed on a variety of integrated material platforms. Existing methods to design and simulate TW-MZMs so far strongly rely on the peculiar material properties, and thus inevitably involve complicated electrical-circuit models. As a result, these methods diverge significantly. In addition, they become increasingly inefficient and inaccurate for TW-MZMs with extending length and levitating modulation speed, posing formidable challenges for millimeter-wave and terahertz operation. Here, we present an innovative perspective to understand and analyze high-speed TW-MZMs. Our perspective leverages nonlinear optics and complex band structures of RF photonic crystals, and is thus entirely electromagnetic-wave-based. Under this perspective, we showcase the design, optoelectronic simulation and experimental validation of high-speed TW-MZMs based on Si and LiNbO<sub>3</sub>, and further demonstrate unambiguous advantages in simplicity, accuracy and efficiency over conventional methods. Our approach can essentially be applied to nearly any integrated material platform, including those based on semiconductors and electro-absorption materials. With high-frequency electrode designs and optoelectronic co-simulation, our approach facilitates the synergy and convergence of electronics and photonics, and offers a viable route to constructing future high-speed millimeter-wave and terahertz photonics and quantum systems.

## INTRODUCTION

Optical modulators [1, 2], which encode information into lightwaves, are pivotal in optical systems and applications such as optical communication [3, 4], quantum information [5, 6], and photonic computing [7, 8]. High-speed modulators can vastly boost signal transmission rates over optical fibers [9, 10]. Equally important, for emerging photonics-accelerated artificial intelligence and neural networks [11–14], optical modulators play a decisive role in multiplication and nonlinear activation in these systems. Innovative photonic computing architectures, such as photonic–electronic deep neural networks [15], photonic tensor processing units [16], and time-wavelength multiplexing [17–20], utilize modulators to achieve computing speeds far exceeding tera-operations per second (TOPS) and currently approaching peta-operations per second (POPS). Functioning as dot-product cells in matrix arrays within cross-bar schemes [21, 22], optical modulators have achieved remarkable computational accuracy up to 99%. Additionally, high-speed modulators enable ultrafast analogue computing functions such as temporal integration and differentiation. These functions endow reconfigurability to multi-purpose microwave photonic processing engines [23, 24].

Among all types of optical modulators, travelling-wave Mach-Zehnder modulators (TW-MZMs) are the most widely deployed. TW-MZMs offer advantages includ-

ing reduced thermal sensitivity compared to resonator-based modulators [25, 26], and simplified RF connection compared to lumped MZMs with segmented electrodes [27, 28]. Especially, with progressing wafer-level micro-fabrication technology and emerging nonlinear materials, high-speed TW-MZMs have been developed on various integrated platforms including silicon (Si) [29, 30], lithium niobate (LiNbO<sub>3</sub>) [31, 32], lithium tantalate (LiTaO<sub>3</sub>) [33, 34], barium tantalate (BaTiO<sub>3</sub>) [35, 36], III-V semiconductors [37, 38], electro-optic polymers [39, 40] and 2D materials [41, 42]. As such, diverse designs of TW-MZMs have been demonstrated to accommodate and exploit material properties. However, these designs differ vastly, particularly in their electrical-circuit models that mimic the materials’ response. For instance, the circuit model for graphene-based TW-MZMs uses the Kubo formula, which relates to the Fermi level, temperature, and other factors [42]. In contrast, the circuit model for Si TW-MZMs must account for the nonlinear current-voltage (I-V) relations of PN junctions [2].

Critical to TW-MZM designs is the RF electrode that determines modulation speed or bandwidth. Successful electrode designs should simultaneously achieve low loss (optical and RF), impedance matching, and group index matching. Among existing electrode designs, the periodic T-shaped electrodes are often favoured. By minimizing RF loss and enabling closer spacing, periodic T-shaped electrodes can overcome the voltage-bandwidth limit in

LiNbO<sub>3</sub> TW-MZMs [43–47]. The slow-wave effect facilitates group index matching between RF and optical waves in Si TW-MZMs [48–51].

Conventionally, designing and modelling periodic T-shaped electrodes have relied on closed-form expressions [51] or  $S$ -parameters [43–50]. However, both approaches are inefficient or inaccurate. The former approach employs conformal mapping to determine electrode capacitance, which becomes increasingly inefficient for complex geometries [52]. Additionally, the expression of resistance and inductance becomes inaccurate at high frequency due to the skin effect [53]. The latter approach requires numerical simulation of long electrodes, e.g., 1000  $\mu\text{m}$  in Ref. [47]. This costs excessive computational resources at frequencies exceeding 100 GHz [30–32] to 500 GHz [47].

In parallel, conventional optoelectronic co-simulation is executed to validate electrode designs, which, however, also has limitations. The segmented-circuit approach divides optical waveguides and RF electrodes into multiple equivalent circuits with delay intervals, and simulates them in Verilog-A [54, 55] or SPICE [56]. This approach is inaccurate due to the different physics between I-V and wave signals. The transmission-line-circuit (TLC) approach requires numerically solving the electrode’s I-V equations combined with PN junctions [57, 58], and thus is inefficient. In both approaches, computationally heavy convolution is necessitated to account for the electrode’s dispersion.

Here, we present an innovative perspective to understand and analyze high-speed TW-MZMs. Our perspective overcomes the above-mentioned inaccuracy and inefficiency in the design and simulation of TW-MZMs, and can be universally applied to any integrated material platforms. Our perspective is rooted in nonlinear optics [59, 60] and complex band structures (CBS) in photonic crystals [61, 62], both of which are derived from Maxwell’s equations – the “first principles” of electromagnetic waves. We view the modulators as *nonlinear RF photonic-crystal waveguides* – a paradigm shift from conventional electrical-circuit models to a fully electromagnetic-wave model. With this perspective, we showcase a unified design and simulation process for Si and LiNbO<sub>3</sub> TW-MZMs. We develop a CBS-based simulation method and demonstrate a 100-times simulation speedup on LiNbO<sub>3</sub> TW-MZMs of 500 GHz bandwidth. We further establish a nonlinear-optics-based optoelectronic co-simulation that obviates computationally heavy I-V equations for PN junctions and convolution calculations. Finally, we present a co-simulated eye diagram for bidirectional RF and optical waves and experimental validation.

## PRINCIPLES OF TRAVELLING-WAVE MACH-ZEHNDER MODULATORS

Figure 1(a,c) presents the cross-sections of a Si TW-MZM with ground-signal (GS) RF electrode, and an x-cut LiNbO<sub>3</sub> TW-MZM with ground-signal-ground (GSG) RF electrodes. Figure 1(b,d) depicts the schematics and layouts of the Si and LiNbO<sub>3</sub> TW-MZMs, including their periodic T-shaped RF electrodes (formed by an array of unit cells) and optical waveguides. The Mach-Zehnder interferometer (MZI) consists of two multimode interferometers (MMI) and two optical waveguide arms. Amplitude modulation of optical signal is achieved via tuning the phase difference between the MZI’s two arms. When voltage is applied between the G and S electrodes, phase difference is induced due to refractive index change of optical waveguides. For Si TW-MZMs, an array of PN junctions in the lateral push-pull configuration is sandwiched by the GS electrodes. When alternating voltage is applied on the GS electrodes, the electron and hole’s distribution in the PN junctions alters accordingly, which changes the refractive index of the Si waveguides due to the plasma dispersion effect. For LiNbO<sub>3</sub> TW-MZMs, the refractive index of LiNbO<sub>3</sub> waveguides is varied due to the Pockels effect.

Here, we interpret the operational principle of Si and LiNbO<sub>3</sub> TW-MZMs as following. The RF electrodes are treated as *periodic sub-wavelength grating waveguides* [62], where the RF wave propagates. Thus the dispersion of RF waveguides (electrodes) is naturally addressed by deriving the RF wave’s group velocity in the waveguide. This treatment avoids conventionally required, complicated convolution calculation [54–58]. For Si TW-MZMs, the array of PN junctions is treated as an *equivalent, fourth-order nonlinear RF material* (i.e., with permittivity and conductivity), by replacing the nonlinear I-V equations of PN junctions with self- and cross-phase modulation (SPM and XPM) of the RF pump. In this perspective, optical modulation in TW-MZMs is a direct consequence of nonlinear interaction between the RF (as the pump) and optical waves (as the signal). Therefore, a universal theoretical framework based on nonlinear optics is capable of modelling TW-MZMs on nearly any material platform besides Si and LiNbO<sub>3</sub>.

In this framework, the TW-MZM design process involves four steps as illustrated in Fig. 1(e) grey box. First, we use temporal coupled-mode equations (TCME) – derived from Maxwell’s equations – to describe nonlinear interaction between RF and optical waves. Second, coefficients in TCME are determined using optical and RF eigenmode solvers. For Si TW-MZMs, the eigenmode solvers require extra semiconductor simulation. Third, a numerical algorithm solves the differential-form TCME in a time-space mesh grid. Finally, with a digital input signal, the simulation results in the eye diagram. In the following sections, we illustrate each step in details.

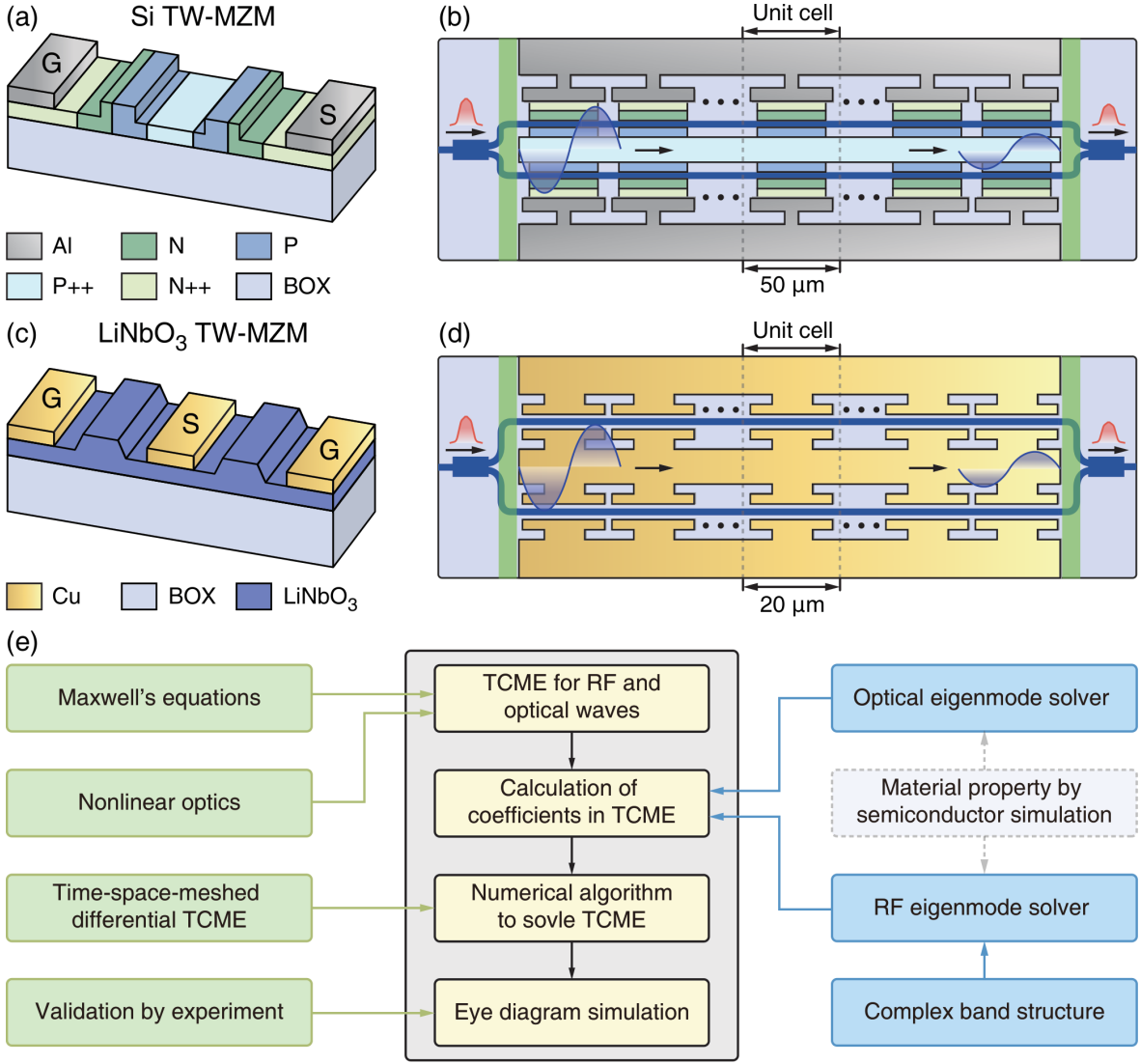


Figure 1. Schematics, layouts and our design process of Si and LiNbO<sub>3</sub> TW-MZMs. (a, c) Cross-sections of the Si TW-MZM with GS RF electrodes (a), and the x-cut LiNbO<sub>3</sub> TW-MZM with GSG electrodes (c). (b,d) Schematics and layouts of the Si (b) and LiNbO<sub>3</sub> (d) TW-MZMs, including their periodic T-shaped RF electrodes and optical waveguides. The electrode's unit cell is outlined within dashed boxes, and the green regions represent the RF wave's input ports and absorbers at output. (e) Our process flowchart to design and simulate high-speed TW-MZMs.

## TEMPORAL COUPLED-MODE EQUATIONS

We use temporal coupled-mode equations (TCME) to describe the nonlinear interaction between RF and optical waves, which are both electromagnetic waves but with vastly different frequencies. Table I summarizes the definition of each symbol used to derive TCME. In a TW-MZM, we consider one static electric field  $E_{dc}$  induced by the bias voltage  $V_{dc}$ , one optical wave  $E_{opt}$  with amplitude  $A_{opt}$ , and one forward RF wave with amplitude  $A_{rf,F}$ . The RF and optical waves experience attenuation ( $\alpha_{rf}$  and  $\alpha_{opt}$ ) during propagation. Caused by impedance mismatch, the forward RF wave is accompanied by a reflected RF wave with amplitude  $A_{rf,R}$ . The forward and

reflected RF waves share the same electric field  $E_{rf}$ . Note that  $E_{dc}$ ,  $E_{opt}$ , and  $E_{rf}$  are all dominant components of the normalized electric field distribution. The TCME for  $A_{opt}$ ,  $A_{rf,F}$  and  $A_{rf,R}$  are

$$\left( \frac{\partial}{\partial z} + \alpha_{rf} + \frac{1}{v_{g,rf}} \frac{\partial}{\partial t} \right) A_{rf,F} = P_{rf,F}^{(2)} + P_{rf,F}^{(3)} + P_{rf,F}^{(4)}, \quad (1a)$$

$$\left( -\frac{\partial}{\partial z} + \alpha_{rf} + \frac{1}{v_{g,rf}} \frac{\partial}{\partial t} \right) A_{rf,R} = P_{rf,R}^{(2)} + P_{rf,R}^{(3)} + P_{rf,R}^{(4)}, \quad (1b)$$

$$\left( \frac{\partial}{\partial z} + \alpha_{opt} + \frac{1}{v_{g,opt}} \frac{\partial}{\partial t} \right) A_{opt} = P_{opt}^{(2)} + P_{opt}^{(3)}. \quad (1c)$$

Here, we designate that RF and optical waves propagate in the  $z$ -direction, thus  $A_{\text{opt}}$ ,  $A_{\text{rf,F}}$ , and  $A_{\text{rf,R}}$  are  $z$ -dependent. The derivation of Eq. (1a–1c) is found in Supplementary Note 1. The reason why the fourth-order nonlinear term  $P_{\text{opt}}^{(4)}$  is neglected in Eq. (1c) is illustrated later with Eq. (8a).

Next, we obtain the  $P_{\text{rf,F}}^{(m)}$  (where  $m = 2, 3, 4$ ) terms in Eq. (1a). Since RF frequency mixing is negligible in TW-MZMs, we only consider SPM and XPM for  $A_{\text{rf,F}}$ . Meanwhile, small RF impedance mismatch (i.e.  $Z_c \approx 50 \Omega$ ) can be easily achieved in practice, leading to  $A_{\text{rf,R}} < A_{\text{rf,F}}$ . Therefore, XPM on  $A_{\text{rf,F}}$  due to  $A_{\text{rf,R}}$  can be ignored. Meanwhile, moderate optical power in TW-MZMs is insufficient to induce nonlinear optical processes such as four-wave mixing and harmonic generation, thus  $A_{\text{rf,F}}$  is not affected by  $A_{\text{opt}}$ . Overall, the  $P_{\text{rf,F}}^{(m)}$  terms including the bias caused by  $V_{\text{dc}}$  and SPM of  $A_{\text{rf,F}}$  can be expressed as

$$\begin{cases} P_{\text{rf,F}}^{(2)} = 2i\Lambda_{\text{dr},12}V_{\text{dc}}A_{\text{rf,F}} , \\ P_{\text{rf,F}}^{(3)} = 3i\Lambda_{\text{r},4}|A_{\text{rf,F}}|^2 A_{\text{rf,F}} + 3i\Lambda_{\text{dr},22}V_{\text{dc}}^2 A_{\text{rf,F}} , \\ P_{\text{rf,F}}^{(4)} = 12i\Lambda_{\text{dr},14}V_{\text{dc}}|A_{\text{rf,F}}|^2 A_{\text{rf,F}} + 4i\Lambda_{\text{dr},32}V_{\text{dc}}^3 A_{\text{rf,F}} , \end{cases} \quad (2)$$

where  $i$  is the imaginary unit. The  $\Lambda$  coefficients are defined as

$$\Lambda_{\text{drp},\text{hjk}} \equiv \iint dx dy \varepsilon_0 \chi^{(h+j+k-1)} E_{\text{dc}}^h E_{\text{rf}}^j E_{\text{opt}}^k . \quad (3)$$

The integration is over the TW-MZM's cross-section ( $xy$ -plane), and the exponents  $(h, j, k) \in \mathbb{N}$ . The subscript  $(d, r, p)$  marks whether  $E_{\text{dc}}$  (labeled with d),  $E_{\text{rf}}$  (labeled with r) and  $E_{\text{opt}}$  (labeled with p) are involved. We also stipulate that if any of  $(h, j, k)$  is zero, the corresponding indices  $(d, r, p)$  are omitted. For example,

$$\begin{cases} \Lambda_{\text{dp},12} = \iint dx dy \varepsilon_0 \chi^{(2)} E_{\text{dc}} E_{\text{opt}}^2 , \\ \Lambda_{\text{r},4} = \iint dx dy \varepsilon_0 \chi^{(3)} E_{\text{rf}}^4 . \end{cases} \quad (4)$$

Additionally,  $(h + j + k - 1) = 2, 3,$  and  $4$  correspond to  $\chi^{(2)}, \chi^{(3)}$  and  $\chi^{(4)}$  processes, respectively.

The  $P_{\text{rf,R}}^{(m)}$  terms in Eq. (1b) can be expressed as

$$\begin{cases} P_{\text{rf,R}}^{(2)} = 2i\Lambda_{\text{dr},12}V_{\text{dc}}A_{\text{rf,R}} , \\ P_{\text{rf,R}}^{(3)} = 3i\Lambda_{\text{r},4}|A_{\text{rf,R}}|^2 A_{\text{rf,R}} + 3i\Lambda_{\text{dr},22}V_{\text{dc}}^2 A_{\text{rf,R}} \\ \quad + 6i\Lambda_{\text{r},4}|A_{\text{rf,F}}|^2 A_{\text{rf,R}} , \\ P_{\text{rf,R}}^{(4)} = 12i\Lambda_{\text{dr},14}V_{\text{dc}}|A_{\text{rf,R}}|^2 A_{\text{rf,R}} + 4i\Lambda_{\text{dr},32}V_{\text{dc}}^3 A_{\text{rf,R}} \\ \quad + 24i\Lambda_{\text{dr},14}V_{\text{dc}}|A_{\text{rf,F}}|^2 A_{\text{rf,R}} . \end{cases} \quad (5)$$

Here we keep the terms  $6i\Lambda_{\text{r},4}|A_{\text{rf,F}}|^2 A_{\text{rf,R}}$  and  $24i\Lambda_{\text{dr},14}V_{\text{dc}}|A_{\text{rf,F}}|^2 A_{\text{rf,R}}$  that describe XPM on  $A_{\text{rf,R}}$  due to  $A_{\text{rf,F}}$ .

The  $P_{\text{opt}}^{(m)}$  terms in Eq. (1c) can be expressed as

$$\begin{cases} P_{\text{opt}}^{(2)} = 2i\Lambda_{\text{dp},12}V_{\text{dc}}A_{\text{opt}} + 2i\Lambda_{\text{rp},12}(V_{\text{rf,F}} + V_{\text{rf,R}})A_{\text{opt}} , \\ P_{\text{opt}}^{(3)} = 3i\Lambda_{\text{dp},22}V_{\text{dc}}^2 A_{\text{opt}} + 3i\Lambda_{\text{rp},22}(V_{\text{rf,F}} + V_{\text{rf,R}})^2 A_{\text{opt}} \\ \quad + 6i\Lambda_{\text{rdp},112}V_{\text{dc}}(V_{\text{rf,F}} + V_{\text{rf,R}})A_{\text{opt}} , \end{cases} \quad (6)$$

where the voltage  $V_{\text{rf,F}} / V_{\text{rf,R}}$  of  $A_{\text{rf,F}} / A_{\text{rf,R}}$  along the RF waveguide (electrode) is derived as

$$\begin{cases} V_{\text{rf,F}}(z, t) = A_{\text{rf,F}}(z, t) \exp(i\beta_{\text{rf}}z - i\omega_{\text{rf}}t) + \text{c.c.} \\ V_{\text{rf,R}}(z, t) = A_{\text{rf,R}}(z, t) \exp(-i\beta_{\text{rf}}z - i\omega_{\text{rf}}t) + \text{c.c.} \end{cases} \quad (7)$$

In Eq. (6), all nonlinear terms relating  $A_{\text{rf,F}}$ ,  $A_{\text{rf,R}}$  and  $V_{\text{dc}}$  with  $A_{\text{opt}}$  are kept. This is to account for phase mismatch between the RF and optical waves, since the typical TW-MZM length of a few millimeters is comparable to the RF wavelength. Meanwhile, the optical wave's SPM is ignored due to insufficient optical power.

We note that the computation of  $\Lambda_{\text{drp},\text{hjk}}$  via Eq. (3) is difficult, besides that the value of PN junctions'  $\chi$  is unknown. Instead, the values of  $\Lambda_{\text{drp},\text{hjk}}$  can be obtained as follows. First, discrete values of effective index change  $\Delta n_{\text{eff,rf}}$  and  $\Delta n_{\text{eff,opt}}$  with different  $V_{\text{dc}}$  values are numerically calculated using optical and RF eigenmode solvers. Then polynomial fits of  $\Delta n_{\text{eff,rf}}$  and  $\Delta n_{\text{eff,opt}}$  with  $V_{\text{dc}}$  are performed, as

$$\begin{aligned} \Delta n_{\text{eff,opt}} &= \frac{1}{k_{\text{opt}}} (2\Lambda_{\text{dp},12}V_{\text{dc}} + 3\Lambda_{\text{dp},22}V_{\text{dc}}^2) , \quad (8a) \\ \Delta n_{\text{eff,rf}} &= \frac{1}{k_{\text{rf}}} (2\Lambda_{\text{dr},12}V_{\text{dc}} + 3\Lambda_{\text{dr},22}V_{\text{dc}}^2 + 4\Lambda_{\text{dr},32}V_{\text{dc}}^3) . \quad (8b) \end{aligned}$$

The derivation is found in Supplementary Note 1. In details,  $\Delta n_{\text{eff,opt}}$  versus  $V_{\text{dc}}$  is numerically calculated using an optical eigenmode solver with the Soref and Bennett's equations for Si [63], or with the Pockels effect for LiNbO<sub>3</sub> [64], as illustrated in Supplementary Note 2 and 3. A second-order polynomial fit of  $\Delta n_{\text{eff,opt}}$  versus  $V_{\text{dc}}$  yields the values of  $\Lambda_{\text{dp},12}$  and  $\Lambda_{\text{dp},22}$ . Based on the simulation result in Supplement Materials Note 3, the second-order polynomial fit is sufficient, justifying the omission of  $P_{\text{opt}}^{(4)}$ . We further assume  $\Lambda_{\text{dp},12} = \Lambda_{\text{rp},12}$  and  $\Lambda_{\text{dp},22} = \Lambda_{\text{rp},22} = \Lambda_{\text{drp},112}$ .

The CBS-based RF eigenmode solver to calculate  $\Delta n_{\text{eff,rf}}$  versus  $V_{\text{dc}}$  is illustrated in the next section. Similarly, a third-order polynomial fit of  $\Delta n_{\text{eff,rf}}$  versus  $V_{\text{dc}}$  yields the values of  $\Lambda_{\text{dr},12}$ ,  $\Lambda_{\text{dr},22}$  and  $\Lambda_{\text{dr},32}$ . Considering that RF waves have quasi-TEM field distribution [65], and neglecting dispersion of  $\chi$  from DC to RF, we have  $\Lambda_{\text{r},4} = \Lambda_{\text{dr},22}$  and  $\Lambda_{\text{dr},14} = \Lambda_{\text{dr},32}$ .

Table I. Summary of symbols used in TCME

| Symbol   | Definition  | Symbol   | Definition  |
|--|---|--|---|
| $A_{\text{rf,F}}, A_{\text{rf,R}}, A_{\text{opt}}$ | Forward RF / reflected RF / optical wave's amplitude. | $P_{\text{rf,F}}^{(m)}, P_{\text{rf,R}}^{(m)}, P_{\text{opt}}^{(m)}$ | Forward RF / reflected RF / optical wave's $m^{\text{th}}$ -order nonlinear term. |
| $E_{\text{rf}}, E_{\text{opt}}$                    | RF / optical wave's electric field.                   | $V_{\text{rf,F}}, V_{\text{rf,R}}$                                   | Forward / reflected RF wave's voltage.  |
| $E_{\text{dc}}$                                    | Static electric field.                                | $V_{\text{dc}}$  | Bias voltage.   |
| $\omega_{\text{rf}}, \omega_{\text{opt}}$          | RF / optical wave's angular frequency.                | $k_{0,\text{rf}}, k_{0,\text{opt}}$                                  | RF / optical wave's wave-number.  |
| $\alpha_{\text{rf}}, \alpha_{\text{opt}}$          | RF / optical wave's attenuation.                      | $\beta_{\text{rf}}, \beta_{\text{opt}}$                              | RF / optical wave's phase constant.   |
| $v_{\text{g,rf}}, v_{\text{g,opt}}$                | RF / optical wave's group velocity.                   | $n_{\text{g,rf}}, n_{\text{g,opt}}$                                  | RF / optical wave's group index.  |
| $n_{\text{eff,rf}}, n_{\text{eff,opt}}$            | RF / optical wave's effective index.                  | $n_{\text{r,rf}}, n_{\text{r,opt}}$                                  | RF / optical wave's phase index.  |
| $Z_c$  | RF impedance.   | $\chi^{(m)}$   | $m^{\text{th}}$ -order nonlinear susceptibility.                                  |

### COMPLEX BAND STRUCTURES OF PERIODIC T-SHAPED RF ELECTRODES

High-speed TW-MZMs require minimal attenuation  $\alpha_{\text{rf}}$ , matched impedance  $Z_c = 50 \Omega$ , and matched indices  $n_{\text{r,rf}} = n_{\text{g,opt}}$  (with  $n_{\text{g,opt}} = 3.89$  for Si and 2.25 for LiNbO<sub>3</sub>) [66]. In this section, we present an RF eigenmode solver to numerically compute these parameters. The eigenmodes of Maxwell's equations are computed under Bloch's condition [67]. The solutions are eigenvectors varying with RF frequency, and thus form complex band structures (CBS). With the CBS and field distribution of the eigenmodes (also known as Bloch modes), the values of  $n_{\text{eff,rf}}, n_{\text{r,rf}} = \text{Re}(n_{\text{eff,rf}})$ ,  $\alpha_{\text{rf}}, Z_c, n_{\text{g,rf}}$  and  $\beta_{\text{rf}}$  used in TCME can be acquired.

The CBS is calculated through finite-element simulation (FEM) of weak-form Maxwell's equations [68]. First, to obtain the weak-form Maxwell's equations, we derive the RF vector wave equation as

$$\nabla \times (\nabla \times \mathbf{E}) - k_{0,\text{rf}}^2 \varepsilon_{\text{re}} \mathbf{E} = 0, \quad (9)$$

where  $\varepsilon_{\text{re}} = \varepsilon_{\text{r}} - \sigma / (i\omega_{\text{rf}}\varepsilon_0)$  is the effective relative permittivity,  $\varepsilon_0$  is the vacuum permittivity,  $\varepsilon_{\text{r}}$  is the relative permittivity, and  $\sigma$  is the conductivity. Using Bloch's theorem, the RF electric field is expressed as

$$\mathbf{E} = \mathbf{u} \exp(ik_z z), \quad (10)$$

where  $\mathbf{u}$  is the Bloch mode's field distribution, and  $k_z$  is the eigen-vector's  $z$ -component. Volume integration over the entire simulation region (described later) yields the weak-form Maxwell's equation, as

$$\iint \int dV ((\nabla - ik_z \hat{\mathbf{z}}) \times \mathbf{w}) \cdot ((\nabla + ik_z \hat{\mathbf{z}}) \times \mathbf{u}) - k_{0,\text{rf}}^2 \mathbf{w} \cdot \varepsilon_{\text{re}} \mathbf{u} = 0, \quad (11)$$

where  $\mathbf{w}$  is the finite-element test function of  $\mathbf{u}$  [68]. The derivation is found in Supplementary Note 4. The  $k_z$  is calculated via FEM of Eq. 11 in COMSOL Multiphysics

[68, 69]. Once the electric field is determined, the magnetic field is derived according to Maxwell's equations.

Figure 2(a, b) shows the RF simulation models for the Si and LiNbO<sub>3</sub> TW-MZMs. Due to mirror symmetry, the models contain only half of the electrode's unit cell, to save computation resources. Perfect electric / magnetic conductor (PEC / PMC) condition, marked as green planes in Fig. 2(a, b), is used for mirror symmetry of the GS / GSG electrode. The region dimension is  $(L_x, L_y, L_z) = (1000, 1000, 50) \mu\text{m}$  in Fig. 2(a), and  $(300, 400, 20) \mu\text{m}$  in Fig. 2(b).

Figure 2(c) shows the simulated cross-section of the Si TW-MZM, consisting of two push-pull PN junctions, Metal 1 and 2 (aluminium, Al), and two via holes for electrical connection through the SiO<sub>2</sub> cladding. Beneath the PN junctions is buried SiO<sub>2</sub> (BOX) on a Si substrate. Figure 2(d) illustrates the transformation of the PN junction to an equivalent RF material (see Supplementary Note 2), which spares computationally heavy, 3D semiconductor simulation. The electrode's dimension is depicted in Fig. 2(e), with  $(L_1, L_2, g_1, g_2, w_1, w_2) = (47, 3, 1, 22, 14.5, 200) \mu\text{m}$ . Figure 2(f) shows the simulated cross-section of the LiNbO<sub>3</sub> TW-MZM with copper (Cu) electrodes. We use loss tangent values of  $\tan\delta = 0.006$  for SiO<sub>2</sub> and 0.008 for LiNbO<sub>3</sub>, following Ref. [70]. Figure 2(g) presents the T-shaped GSG electrodes. The S and G electrodes share the same dimension  $(L_1, L_2, g_1, g_2, w_1, w_2) = (18, 14, 5.5, 3, 2, 25) \mu\text{m}$ . The ridge / slab thickness is 220 / 90 nm for PN junctions, and 500 / 250 nm for LiNbO<sub>3</sub>. Both the PN junctions and LiNbO<sub>3</sub> are treated as thin-layer boundary condition (see Supplementary Note 4).

With simulated  $k_z$ , we have  $\beta_{\text{rf}} = \text{Re}(k_z)$ ,  $\alpha_{\text{rf}} = \text{Im}(k_z)$ ,  $n_{\text{eff,rf}} = k_z / k_{0,\text{rf}}$ ,  $n_{\text{r,rf}} = \text{Re}(n_{\text{eff,rf}})$ ,  $n_{\text{g,rf}} = c\beta_{1,\text{rf}}$ , where  $\beta_{1,\text{rf}}$  is the first-order Taylor expansion of  $\beta_{\text{rf}}(\omega_{\text{rf}})$ . Thus, the assumption of  $n_{\text{g,rf}} \approx n_{\text{r,rf}}$  in Ref. [29, 49] is inaccurate. Then  $Z_c = V^2 / P_z$  is calculated, where

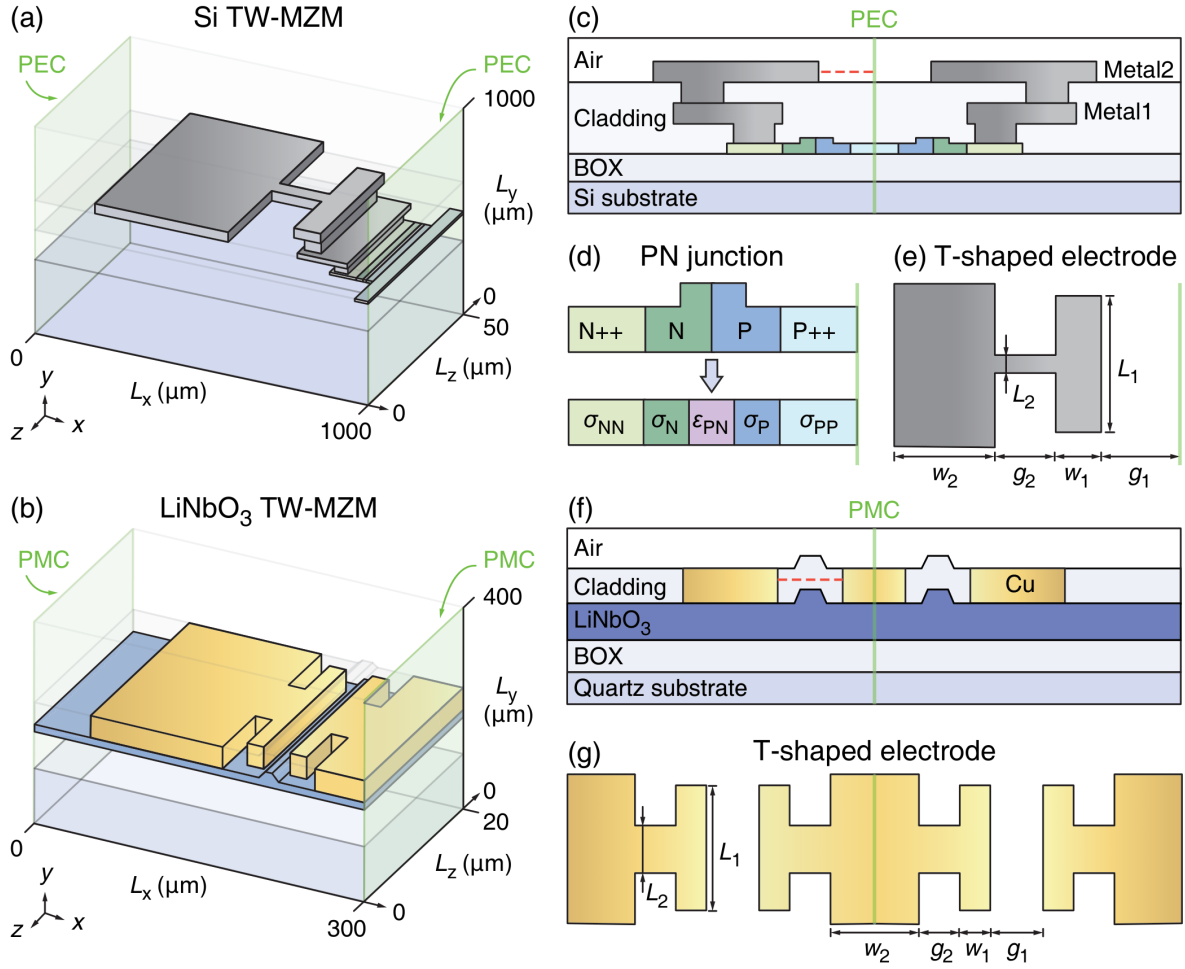


Figure 2. Simulation models of periodic T-shaped RF electrodes. (a,b) RF simulation models for Si (a) and LiNbO<sub>3</sub> (b) TW-MZMs with half of the electrode's unit cell. Green planes are PEC (a) or PMC (b) boundary condition. Other boundary planes are set as periodic condition. (c,f) Cross-section and layer structure of Si (c) and LiNbO<sub>3</sub> (f) TW-MZMs. (d) The transformation of the PN junction to an equivalent RF material with permittivity and conductivity. (e, g) Layout and dimension of the unit cell of periodic T-shaped electrodes for Si (GS, c) and LiNbO<sub>3</sub> (GSG, f) TW-MZMs.

$$P_z = 2 \iint_S dx dy S_z \quad (12a)$$

$$V = \begin{cases} \int_C dx E_x, & \text{with GSG electrodes} \\ 2 \int_C dx E_x, & \text{with GS electrodes} \end{cases} \quad (12b)$$

The surface  $S$  in Eq. (12a) covers the simulation region's cross-section at  $L_z = 0 \mu\text{m}$ , and  $S_z$  is the  $z$ -component of the Poynting vector. Since  $V$  is path-independent for a quasi-TEM field, the path curve  $C$  in Eq. (12b) is chosen as the red dashed lines in Fig. 2(a, b).

For Si TW-MZMs, Fig. 3(a-c) presents the simulation results of  $n_{r,\text{rf}}$ ,  $Z_c$  and  $\alpha_{\text{rf}}$ , with varying  $V_{\text{dc}}$  and  $\omega_{\text{rf}}/2\pi = 10, 20, 30$  GHz. The conditions  $n_{r,\text{rf}} = n_{g,\text{opt}} = 3.89$  and  $Z_c = 50 \Omega$  are satisfied at  $V_{\text{dc}} = -3$  V and  $\omega_{\text{rf}}/2\pi = 20$

GHz. Parameter sweep of  $\omega_{\text{rf}}/2\pi \in [10, 120]$  GHz and  $V_{\text{dc}} \in [-6, 0]$  V is found in Supplementary Note 4.

For LiNbO<sub>3</sub> TW-MZMs, Fig. 3(d, e) presents the simulation results of  $n_{r,\text{rf}}$  and  $Z_c$  with varying  $\omega_{\text{rf}}/2\pi \in [20, 500]$  GHz and  $L_2 = 12, 14, 16 \mu\text{m}$ . Suggested by Fig. 3(d, e), we select  $L_2 = 14 \mu\text{m}$  for  $n_{r,\text{rf}} = n_{g,\text{opt}} = 2.25$  and  $Z_c = 50 \Omega$  at  $\omega_{\text{rf}}/2\pi = 400$  GHz. Figure 3(f) shows the impact of electrode materials on  $\alpha_{\text{rf}}$ , i.e. gold (Au) with  $\tan\delta$ , Cu with  $\tan\delta$ , and Cu without  $\tan\delta$ . As Cu ( $\sigma_{\text{Cu}} \approx 5.8 \times 10^7$  S/m) has higher conductivity than Au ( $\sigma_{\text{Au}} \approx 4.5 \times 10^7$  S/m), Cu electrodes enable lower RF attenuation (smaller  $\alpha_{\text{rf}}$ ). Meanwhile,  $\tan\delta$  of SiO<sub>2</sub> and LiNbO<sub>3</sub> increases  $\alpha_{\text{rf}}$  for  $\omega_{\text{rf}}/2\pi > 100$  GHz. The electric ( $E_x$ ) and magnetic ( $H_x$  and  $H_y$ ) fields of Si and LiNbO<sub>3</sub> TW-MZMs are found in Supplementary Note 4.

We also simulate the electrode design in Ref. [47] and obtain  $n_{r,\text{rf}} = 2.26$ ,  $\alpha_{\text{rf}} = 13$  dB/cm and  $Z_c = 46 \Omega$  with  $\omega_{\text{rf}}/2\pi = 300$  GHz. These values closely match the ex-

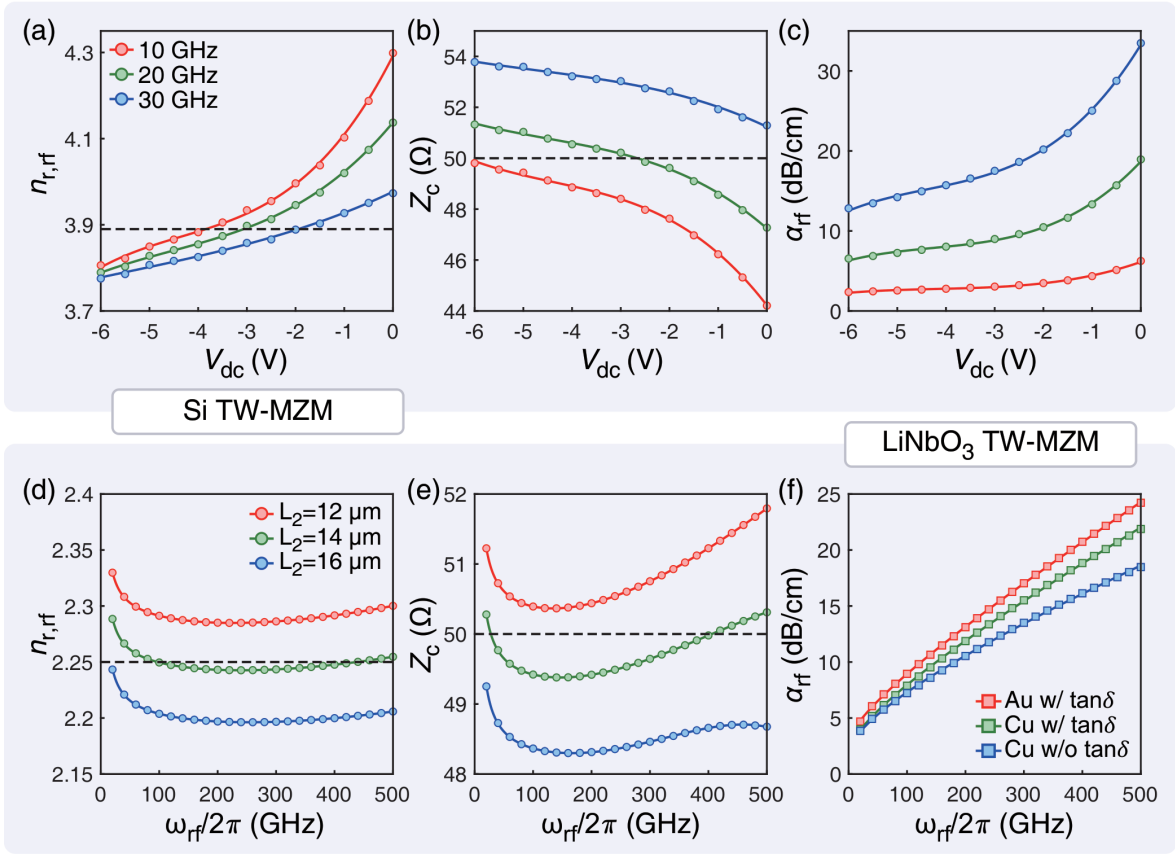


Figure 3. Simulation results of periodic T-shaped RF electrodes. (a-c) Calculated  $n_{r,rf}$ ,  $Z_c$  and  $\alpha_{rf}$  with varying  $V_{dc}$  and  $\omega_{rf}/2\pi = 10, 20, 30$  GHz, for Si TW-MZMs. (d, e) Calculated  $n_{r,rf}$  and  $Z_c$  with varying  $\omega_{rf}/2\pi \in [20, 500]$  GHz and  $L_2 = 12, 14, 16$   $\mu\text{m}$ , for LiNbO<sub>3</sub> TW-MZMs. (f) With  $L_2 = 14$   $\mu\text{m}$  and  $\omega_{rf}/2\pi \in [20, 500]$  GHz, the calculated  $\alpha_{rf}$  of Au with  $\tan\delta$ , Cu with  $\tan\delta$ , and Cu without  $\tan\delta$ .

perimental result of  $n_{r,rf} = 2.26$ ,  $\alpha_{rf} = 14$  dB/cm and  $Z_c = 46$   $\Omega$  in Ref. [47]. Further validations are provided in Supplementary Note 8. Compared to the simulation of 1000- $\mu\text{m}$ -long electrodes in Ref. [47], here we only simulate half of a 20- $\mu\text{m}$ -long unit cell. Our simulation saves substantial computational resources and is more than 100 times faster.

### OPTOELECTRONIC CO-SIMULATION TO SOLVE TCME

With the acquired coefficients via eigenmode solvers, we next numerically solve the TCME Eq. (1a–1c) using optoelectronic co-simulation. Figure 4 delineates the numerical algorithms to calculate  $A_{rf,F}$ ,  $A_{rf,R}$  and  $A_{opt}$ . Figure 4(a) shows the periodic T-shaped RF electrodes as an RF waveguide. The green regions mark the boundary condition (see Supplementary Note 5). We use two time-space mesh grids of identical temporal grid size  $\Delta t = 0.5$  ps, sufficiently small to achieve numerical convergence. Thus, the spatial grid sizes are different given by the different wave speeds, i.e.  $\Delta z_{rf} = v_{g,rf}\Delta t$  and

$\Delta z_{opt} = v_{g,opt}\Delta t$ . Figure 4(b) depicts the 2D mesh grid used to solve the RF TCME Eq. (1a, 1b). Each circle represents a node storing the values of  $A_{rf,F}$  and  $A_{rf,R}$ , whose initial values are zero. Black and gray arrows mark the calculation sequence. Green arrows mark the boundary condition. Orange arrows mark the input voltage signal  $V_{in}$ .

The algorithm starts with the calculation of  $A_{rf,F}$ , which is stimulated by  $V_{in}$  via the left boundary condition and follows the black arrows. The calculation of  $A_{rf,R}$  is triggered by  $A_{rf,F}$  on the right boundary condition due to impedance mismatch. Ultimately, the algorithm yields the distribution of  $V_{rf,F}$  and  $V_{rf,R}$  on the mesh grid based on Eq. (7).

Figure 4(c) shows that the input optical wave  $A_{opt,in}$  is divided into  $A_{opt,1}$  and  $A_{opt,2}$  in the MZI's two arms. Black arrows mark the sequence to calculate  $A_{opt,1}$  and  $A_{opt,2}$ . Cyan arrows represent Eq. (6). For brevity, we use  $V_{rf}$  to represent  $V_{rf,F}$ ,  $V_{rf,R}$  and  $V_{dc}$ . Since  $\Delta z_{opt} \neq \Delta z_{rf}$ , we use interpolation to re-sample the distribution of  $V_{rf}$  along the  $z$ -direction, consistent with the 2D mesh grid used to calculate  $A_{opt,1}$  and  $A_{opt,2}$ . As  $\omega_{opt} \gg \omega_{rf}$ , instead of using a finer grid size  $\Delta z_{opt}$ , we

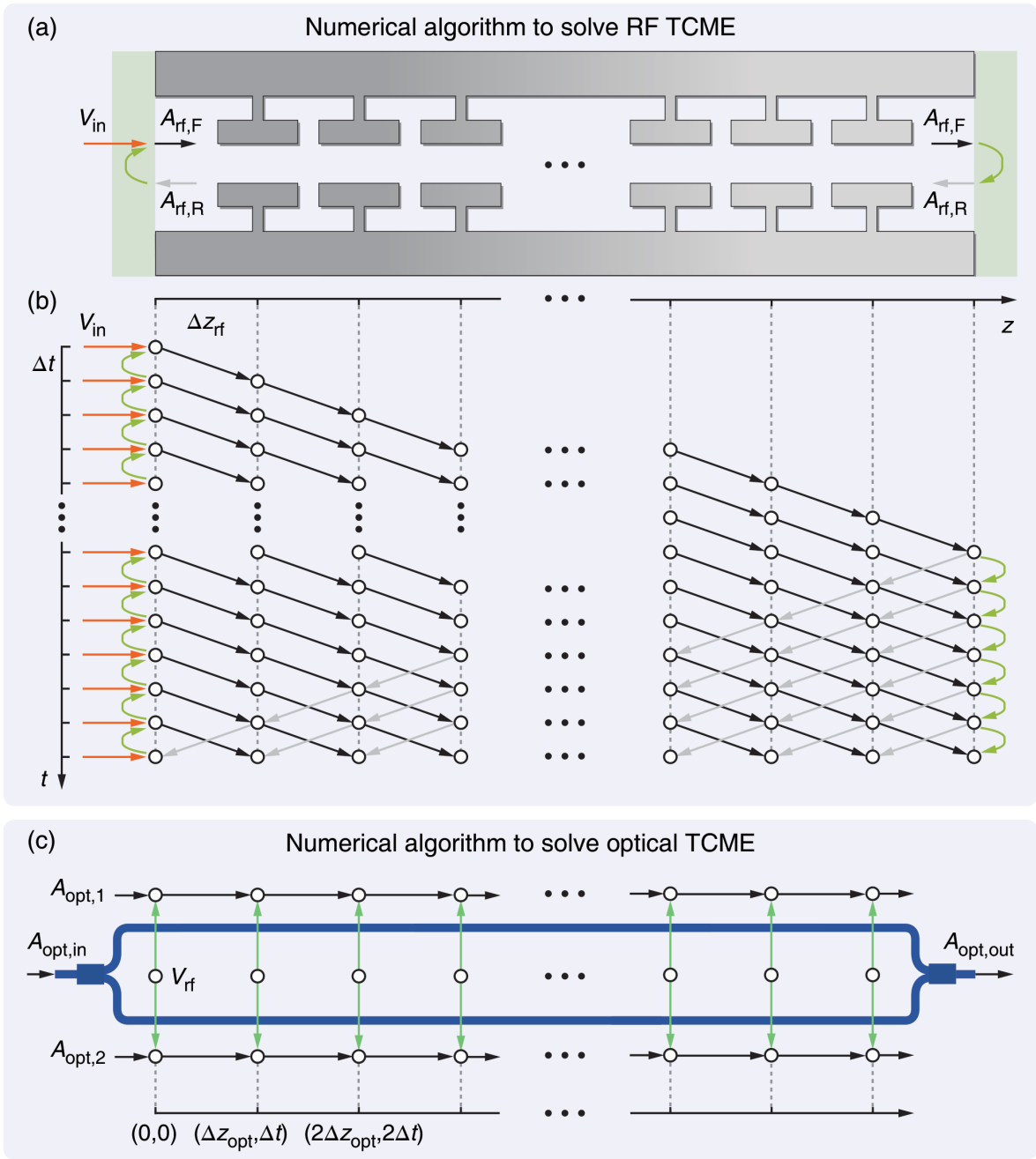


Figure 4. Optoelectronic co-simulation to solve TCME. (a) Numerical algorithm to solve the RF TCME. Green regions mark the boundary condition for  $A_{rf,F}$  and  $A_{rf,R}$ . (b) 2D time-space mesh grid to solve the RF TCME. Each circle represents a node storing the values of  $A_{rf,F}$  and  $A_{rf,R}$ . Black and gray arrows mark the sequence to calculate  $A_{rf,F}$  and  $A_{rf,R}$ . Green arrows mark the boundary condition. Orange arrows mark the input voltage signal  $V_{in}$ . (c) Numerical algorithm to solve the optical TCME. The input optical wave  $A_{opt,in}$  is divided into  $A_{opt,1}$  and  $A_{opt,2}$ . Black arrows mark the sequence to calculate  $A_{opt,1}$  and  $A_{opt,2}$ . Here  $V_{rf}$  to represent  $V_{rf,F}$ ,  $V_{rf,R}$  and  $V_{dc}$ , and cyan arrows represent nonlinearity terms of  $V_{rf}$ .

use an equivalent approach to transform the differential form of  $A_{opt,1}$  and  $A_{opt,2}$  into the exponential differential form. The output optical wave is  $A_{opt,out}$  recombining  $A_{opt,1}$  and  $A_{opt,2}$ . The exact differential forms of  $A_{rf,F}$ ,  $A_{rf,R}$ ,  $A_{opt,1}$  and  $A_{opt,2}$  are found in Supplementary Note 6.

## SIMULATION AND EXPERIMENTAL VALIDATION OF EYE DIAGRAMS

Finally, the TW-MZM's eye diagram can be obtained with the solved TCME. In this section, we first elaborate the experimental measurement of a Si TW-MZM,



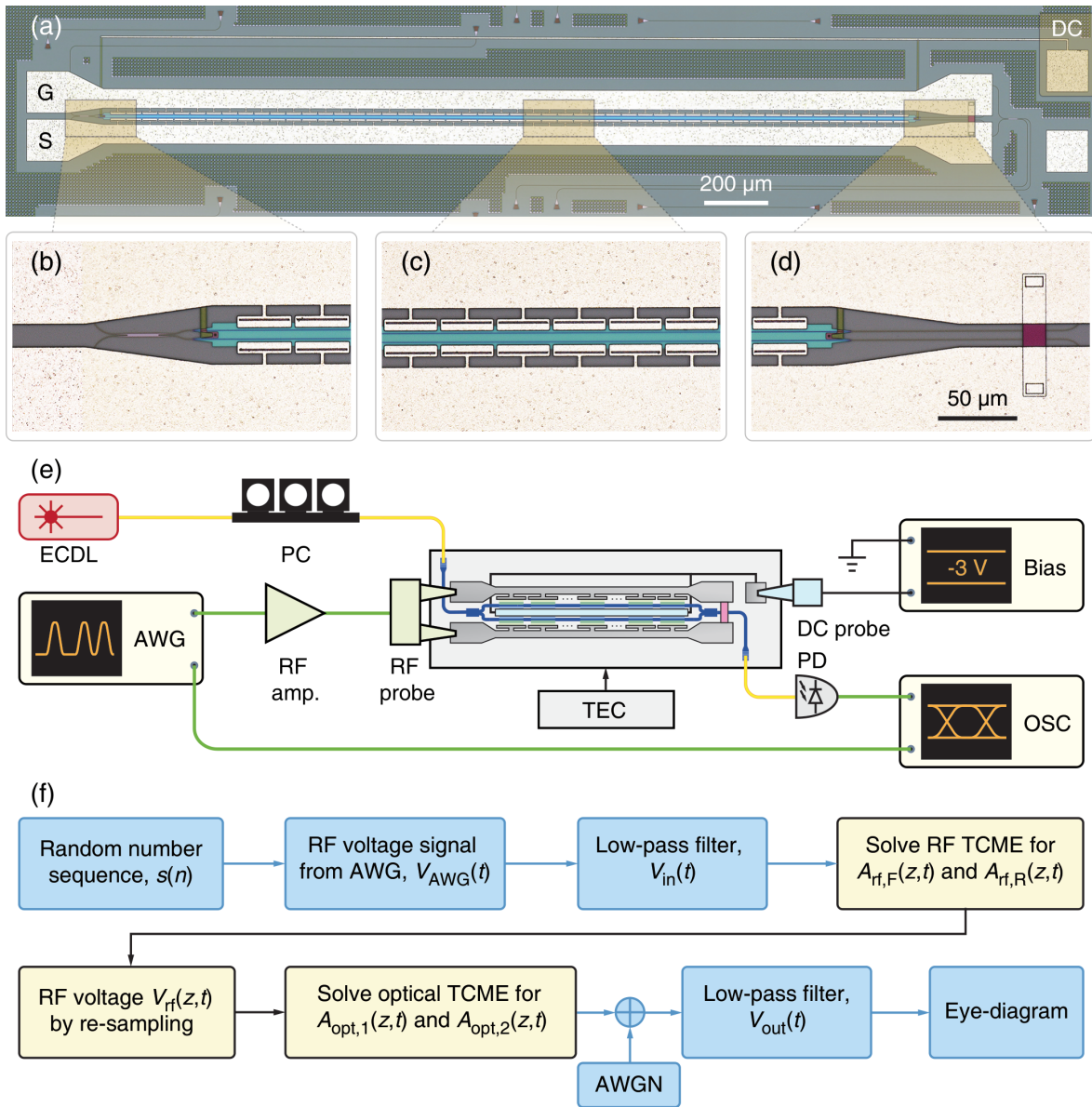


Figure 5. Simulation and experimental validation of eye diagrams. (a) Optical microscope images of a Si TW-MZM. (b-d) Zoom-in views of the Si TW-MZM, highlighting the MMI (b), the electrode's unit cell (c), and the matched resistor (d). (e) Experimental setup to measure eye diagrams of the Si TW-MZM. (f) Simulation flowchart outlining the process for generating eye diagrams.

and then show simulation results that are validated by the experiment. Figure 5(a) shows an optical microscope image of a 2.5-mm-long Si TW-MZM fabricated using a commercial CMOS foundry process. Figure 5(c) highlights the RF electrodes with PN junctions. Figure 5(b) shows the upper and lower electrodes connecting to a GS pad for RF input. Figure 5(d) shows the matched resistor for RF absorption. A length difference of  $100 \mu\text{m}$  between the MZI's two arms enables 3-dB operating point tuning by varying the laser frequency. As shown in Fig. 5(b,d), the DC electrical circuit connects to the P++ region and provides reverse-biased voltage for the

PN junctions.

Figure 5(e) displays the experimental setup for eye-diagram measurement in digital communication using our Si TW-MZM. An arbitrary waveform generator (AWG) serves as the RF source providing non-return-to-zero (NRZ) modulation signals. After RF amplification and transmission in RF cables and probes, the RF peak-to-peak voltage is estimated as  $V_{pp} = 5 \text{ V}$ . The AWG is also connected to and synchronizes an oscilloscope (OSC). A thermo-electric cooler (TEC) maintains the TW-MZM at  $25^\circ\text{C}$ . The DC source supplies  $V_{dc} = -3\text{V}$  bias, with one terminal to ground. The out-

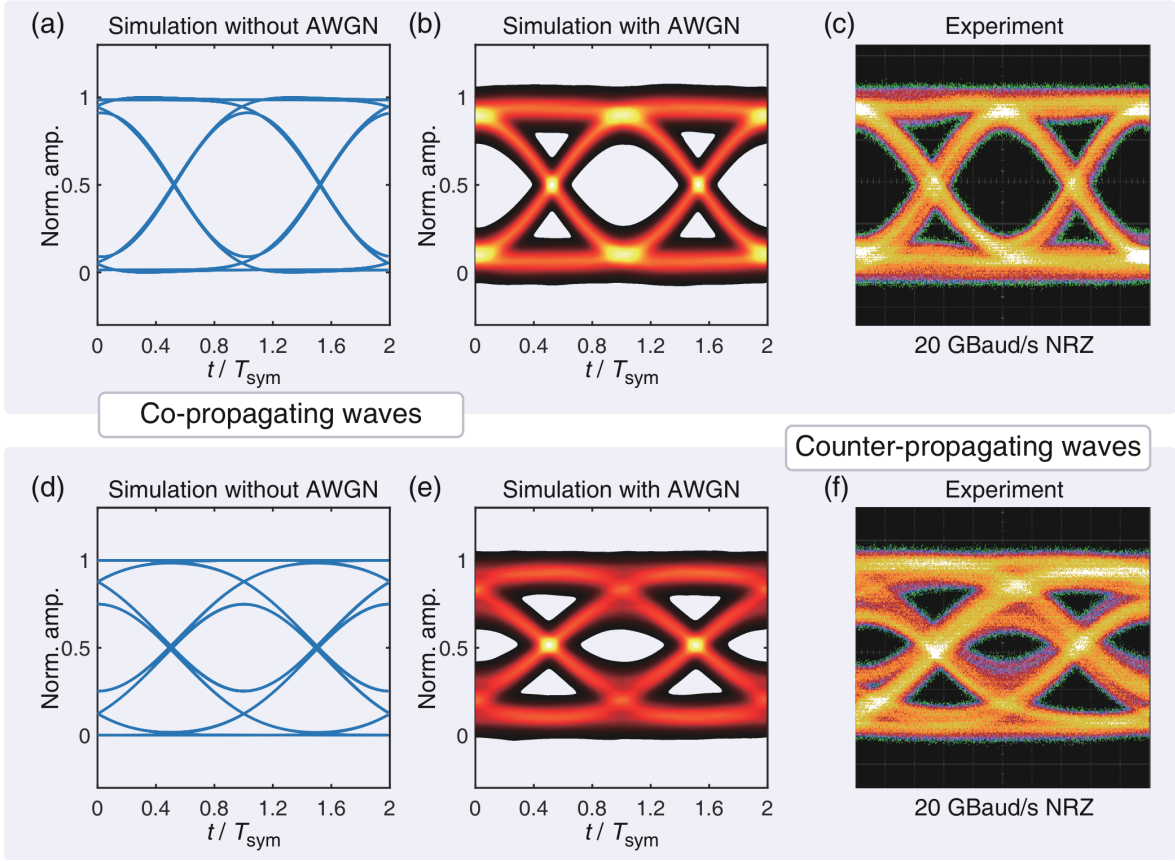


Figure 6. Simulated and experimental eye diagrams. With co-propagating waves, the simulated ER = 6.5 dB and  $Q = 7.5$  in (b) agree with the measured ER = 6.4 dB and  $Q = 7.3$  in (c). With counter-propagating waves, the simulated ER = 4.8 dB and  $Q = 3.3$  in (e) also agree with the measured ER = 4.4 dB and  $Q = 3.2$  in (f).

put wavelength of the external-cavity diode laser (ECDL) is set at the TW-MZM’s operating point of 1549.5 nm. A polarization controller (PC) is used to optimize the input optical signal’s polarization. A photodetector (PD) collects the modulated light from the TW-MZM. The eye diagram is displayed by the OSC and shown in Fig. 6(c, f).

In parallel, we simulate the eye diagram based on the experimental setup. The simulation flow chart is illustrated in Fig. 5(f). We generate NRZ modulation signals from a sequence of random numbers  $s(n)$ . The RF voltage signal  $V_{\text{AWG}}(t)$  is created based on  $s(n)$ . Considering the actual bandwidth of our AWG and RF amplifier, a digital low-pass filter is used to limit the bandwidth of  $V_{\text{AWG}}(t)$  to below 20 GHz. The filtered result is  $V_{\text{in}}(t)$ . With the previously acquired numerical solution of TCME, the values of  $A_{\text{rf,F}}$ ,  $A_{\text{rf,R}}$ ,  $A_{\text{opt,1}}$  and  $A_{\text{opt,2}}$  are input to the eye-diagram simulation. Additive white Gaussian noise (AWGN), characterized by the signal-to-noise ratio (SNR, described latter) [71], is introduced to mimic experimental noise. The signal with AWGN passes through a low-pass filter mimicking the RF bandwidth below 20 GHz of the PD and OSC. The filtered signal is

visualized as an eye diagram by accumulating data within two digital symbol periods  $T_{\text{sym}}$ .

Figure 6 compares the simulated and experimental eye diagrams, for two configurations: the co-propagating optical and RF waves in Fig. 6(a–c), and the counter-propagating waves in Fig. 6(d–f). This bidirectional propagation scheme is widely used in designing Michelson-interferometer modulators [72], modulator-based gyroscopes [73], and isolators [74]. Figure 6(a,d,b,e) shows the simulated eye diagrams without or with AWGN. For counter-propagation waves, the sequence to calculate  $A_{\text{opt,1}}$  and  $A_{\text{opt,2}}$  is reversed as shown in Fig. 4(c). Counter-propagating waves are experimentally realized by interchanging the input (ECDL and PC) with the output (PD and OSC) in Fig. 5(e). Figure 6 evidences that the eye diagram with counter-propagating waves is worse.

In the simulation of co-propagating waves, we set the SNR of AWGN to 22.5 dB. The resulting eye diagram, shown in Fig. 6(b), exhibits 6.5 dB extinction ratio (ER) and a quality factor of  $Q = 7.5$ . These values agree with the experimental result of 6.4 dB ER and  $Q = 7.3$  in Fig. 6(c). Applying the same SNR (22.5 dB) to counter-

propagating waves, the simulated eye diagram in Fig. 6(e) shows a 4.8 dB ER and  $Q = 3.3$ . Again, these values agree with the experimental result of 4.4 dB ER and  $Q = 3.2$  in Fig. 6(f).

## CONCLUSION

In conclusion, we present a universal perspective to understand and analyze high-speed TW-MZMs using nonlinear optics and complex band structures. Under this perspective, we design, simulate and experimentally validate high-speed TW-MZMs based on Si and LiNbO<sub>3</sub>. Our approach shows unambiguous advantages in simplicity, accuracy and efficiency over conventional methods. Detailed comparisons highlighting the key advantages of our method over previous approaches are summarized in Supplementary Note 7. Though showcased on Si and LiNbO<sub>3</sub> TW-MZMs, the proposed method is highly adaptable and can essentially be applied to nearly any integrated material platform. In addition, by considering the imaginary part of nonlinear coefficients, our approach is equally practical for TW-MZMs based on electro-absorption materials such as graphene [75], SiGe [76] and III-V [77]. For integrated semiconductor platforms such as Si, Ge and III-V, this approach based on the equivalent nonlinearity of PN junctions in both the RF and optical domains can be instrumental for nonlinear and quantum microwave photonics [78, 79]. Finally, our optoelectronic co-simulation establishes a wave-based framework, facilitating the synergy and convergence of electronics and photonics. With electrode designs capable of reaching frequencies above 500 GHz, our approach offers a viable route to constructing future high-speed TW-MZMs for millimeter-wave and terahertz applications.

The authors thank Lan Gao, Xue Bai, Baoqi Shi, Jinbao Long, and Yihan Luo for their suggestions on the manuscript. This work was supported by the National Key R&D Program of China (Grants No. 2024YFA1409300), National Natural Science Foundation of China (No. 12261131503, 62405202), Innovation Program for Quantum Science and Technology (2023ZD0301500), Shenzhen Science and Technology Program (No. RCJC20231211090042078), Shenzhen-Hong Kong Cooperation Zone for Technology and Innovation (HZQB-KCZYB2020050), Guangdong-Hong Kong Technology Cooperation Funding Scheme (No. 2024A0505040008). Data underlying the results presented in this paper are not publicly available at this time but may be obtained from the authors upon reasonable request.

\* These authors contributed equally to this work.

† Contact author: [ray.shower19@gmail.com](mailto:ray.shower19@gmail.com)

‡ Contact author: [liujq@iqasz.cn](mailto:liujq@iqasz.cn)

- [1] Q. Xu, B. Schmidt, S. Pradhan, and M. Lipson, *Nature* **435**, 325 (2005).
- [2] G. T. Reed, G. Mashanovich, F. Y. Gardes, and D. J. Thomson, *Nature Photonics* **4**, 518 (2010).
- [3] Q. Cheng, M. Bahadori, M. Glick, S. Rumley, and K. Bergman, *Optica* **5**, 1354 (2018).
- [4] J. Wang and Y. Long, *Science Bulletin* **63**, 1267 (2018).
- [5] P. Sibson, J. E. Kennard, S. Stanisic, C. Erven, J. L. O'Brien, and M. G. Thompson, *Optica* **4**, 172 (2017).
- [6] S. Wehner, D. Elkouss, and R. Hanson, *Science* **362**, eaam9288 (2018).
- [7] Y. Shen, N. C. Harris, S. Skirlo, M. Prabhu, T. Baehr-Jones, M. Hochberg, X. Sun, S. Zhao, H. Larochelle, D. Englund, and M. Soljačić, *Nature Photonics* **11**, 441 (2017).
- [8] W. Bogaerts, D. Pérez, J. Capmany, D. A. B. Miller, J. Poon, D. Englund, F. Morichetti, and A. Melloni, *Nature* **586**, 207 (2020).
- [9] M. Zhang, C. Wang, P. Kharel, D. Zhu, and M. Lončar, *Optica* **8**, 652 (2021).
- [10] Y. Shi, Y. Zhang, Y. Wan, Y. Yu, Y. Zhang, X. Hu, X. Xiao, H. Xu, L. Zhang, and B. Pan, *Photonics Research* **10**, A106 (2022).
- [11] B. J. Shastri, A. N. Tait, T. Ferreira De Lima, W. H. P. Pernice, H. Bhaskaran, C. D. Wright, and P. R. Prucnal, *Nature Photonics* **15**, 102 (2021).
- [12] J. Feldmann, N. Youngblood, M. Karpov, H. Gehring, X. Li, M. Stappers, M. Le Gallo, X. Fu, A. Lukashchuk, A. S. Raja, J. Liu, C. D. Wright, A. Sebastian, T. J. Kippenberg, W. H. P. Pernice, and H. Bhaskaran, *Nature* **589**, 52 (2021).
- [13] C. Huang, V. J. Sorger, M. Miscuglio, M. Al-Qadasi, A. Mukherjee, L. Lampe, M. Nichols, A. N. Tait, T. Ferreira De Lima, B. A. Marquez, J. Wang, L. Chrostowski, M. P. Fok, D. Brunner, S. Fan, S. Shekhar, P. R. Prucnal, and B. J. Shastri, *Advances in Physics: X* **7**, 1981155 (2022).
- [14] N. Farmakidis, B. Dong, and H. Bhaskaran, *Nature Reviews Electrical Engineering* **1**, 358 (2024).
- [15] F. Ashtiani, A. J. Geers, and F. Aflatouni, *Nature* **606**, 501 (2022).
- [16] B. Dong, F. Brückhoff-Plückelmann, L. Meyer, J. Dijkstra, I. Bente, D. Wendland, A. Varri, S. Aggarwal, N. Farmakidis, M. Wang, G. Yang, J. S. Lee, Y. He, E. Gooskens, D.-L. Kwong, P. Bienstman, W. H. P. Pernice, and H. Bhaskaran, *Nature* **632**, 55 (2024).
- [17] X. Xu, M. Tan, B. Corcoran, J. Wu, A. Boes, T. G. Nguyen, S. T. Chu, B. E. Little, D. G. Hicks, R. Morandotti, A. Mitchell, and D. J. Moss, *Nature* **589**, 44 (2021).
- [18] S. Xu, J. Wang, S. Yi, and W. Zou, *Nature Communications* **13**, 7970 (2022).
- [19] B. Bai, Q. Yang, H. Shu, L. Chang, F. Yang, B. Shen, Z. Tao, J. Wang, S. Xu, W. Xie, W. Zou, W. Hu, J. E. Bowers, and X. Wang, *Nature Communications* **14**, 66 (2023).
- [20] Y. Zhu, M. Luo, X. Hua, L. Xu, M. Lei, M. Liu, J. Liu, Y. Liu, Q. Wang, C. Yang, D. Chen, L. Wang, and

- X. Xiao, *Optica* **11**, 583 (2024).
- [21] M. Moralis-Pegios, G. Giamougiannis, A. Tsakyridis, D. Lazovsky, and N. Pleros, *Nature Communications* **15**, 5468 (2024).
- [22] S. Rahimi Kari, N. A. Nobile, D. Pantin, V. Shah, and N. Youngblood, *Optica* **11**, 542 (2024).
- [23] D. Marpaung, J. Yao, and J. Capmany, *Nature Photonics* **13**, 80 (2019).
- [24] H. Feng, T. Ge, X. Guo, B. Wang, Y. Zhang, Z. Chen, S. Zhu, K. Zhang, W. Sun, C. Huang, Y. Yuan, and C. Wang, *Nature* **627**, 80 (2024).
- [25] M. Li, J. Ling, Y. He, U. A. Javid, S. Xue, and Q. Lin, *Nature Communications* **11**, 4123 (2020).
- [26] W. Zhang, M. Ebert, K. Li, B. Chen, X. Yan, H. Du, M. Banakar, D. T. Tran, C. G. Littlejohns, A. Scofield, G. Yu, R. Shafiha, A. Zilkie, G. Reed, and D. J. Thomson, *Nature Photonics* **17**, 273 (2023).
- [27] M. Jacques, Z. Xing, A. Samani, E. El-Fiky, X. Li, M. Xiang, S. Lessard, and D. V. Plant, *Journal of Lightwave Technology*, 2877 (2020).
- [28] A. Mohammadi, Z. Zheng, X. Zhang, L. A. Rusch, and W. Shi, *Journal of Lightwave Technology* **41**, 5059 (2023).
- [29] M. Li, L. Wang, X. Li, X. Xiao, and S. Yu, *Photonics Research* **6**, 109 (2018).
- [30] C. Han, Z. Zheng, H. Shu, M. Jin, J. Qin, R. Chen, Y. Tao, B. Shen, B. Bai, F. Yang, Y. Wang, H. Wang, F. Wang, Z. Zhang, S. Yu, C. Peng, and X. Wang, *Science Advances* **9**, eadi5339 (2023).
- [31] C. Wang, M. Zhang, X. Chen, M. Bertrand, A. Shams-Ansari, S. Chandrasekhar, P. Winzer, and M. Lončar, *Nature* **562**, 101 (2018).
- [32] M. He, M. Xu, Y. Ren, J. Jian, Z. Ruan, Y. Xu, S. Gao, S. Sun, X. Wen, L. Zhou, L. Liu, C. Guo, H. Chen, S. Yu, L. Liu, and X. Cai, *Nature Photonics* **13**, 359 (2019).
- [33] C. Wang, Z. Li, J. Riemensberger, G. Lihachev, M. Churraev, W. Kao, X. Ji, J. Zhang, T. Blesin, A. Davydova, Y. Chen, K. Huang, X. Wang, X. Ou, and T. J. Kippenberg, *Nature* **629**, 784 (2024).
- [34] C. Wang, D. Fang, J. Zhang, A. Kotz, G. Lihachev, M. Churraev, Z. Li, A. Schwarzenberger, X. Ou, C. Koos, and T. J. Kippenberg, *Optica* **11**, 1614 (2024).
- [35] F. Eltes, G. E. Villarreal-Garcia, D. Caimi, H. Siegart, A. A. Gentile, A. Hart, P. Stark, G. D. Marshall, M. G. Thompson, J. Barreto, J. Pompeyrine, and S. Abel, *Nature Materials* **19**, 1164 (2020).
- [36] Z. Dong, A. Raju, A. B. Posadas, M. Reynaud, A. A. Demkov, and D. M. Wasserman, *ACS Photonics* **10**, 4367 (2023).
- [37] P. C. Schindler, D. Korn, C. Stamatiadis, M. O'Keefe, L. Stampoulidis, R. Schmogrow, P. Zakynthinos, R. Palmer, N. Cameron, Y. Zhou, *et al.*, *Journal of Lightwave Technology* **32**, 760 (2013).
- [38] Y. Ogiso, Y. Hashizume, H. Tanobe, N. Nunoya, M. Ida, Y. Miyamoto, M. Ishikawa, J. Ozaki, Y. Ueda, H. Wakita, M. Nagatani, H. Yamazaki, M. Nakamura, T. Kobayashi, and S. Kanazawa, *Journal of Lightwave Technology* **38**, 249 (2020).
- [39] M. Lee, H. E. Katz, C. Erben, D. M. Gill, P. Gopalan, J. D. Heber, and D. J. McGee, *Science* **298**, 1401 (2002).
- [40] G.-W. Lu, J. Hong, F. Qiu, A. M. Spring, T. Kashino, J. Oshima, M.-a. Ozawa, H. Nawata, and S. Yokoyama, *Nature Communications* **11**, 4224 (2020).
- [41] Z. Sun, A. Martinez, and F. Wang, *Nature Photonics* **10**, 227 (2016).
- [42] V. Soriano, M. Midrio, G. Contestabile, I. Asselberghs, J. Van Campenhout, C. Huyghebaert, I. Goykhman, A. K. Ott, A. C. Ferrari, and M. Romagnoli, *Nature Photonics* **12**, 40 (2017).
- [43] P. Kharel, C. Reimer, K. Luke, L. He, and M. Zhang, *Optica* **8**, 357 (2021).
- [44] Z. Wang, G. Chen, Z. Ruan, R. Gan, P. Huang, Z. Zheng, L. Lu, J. Li, C. Guo, K. Chen, and L. Liu, *ACS Photonics* **9**, 2668 (2022).
- [45] F. Valdez, V. Mere, and S. Mookherjea, *Optica* **10**, 578 (2023).
- [46] Y. Du, X. Zou, F. Zou, W. Pan, L. Yan, Q. Zhao, and N. Liu, *Laser & Photonics Reviews*, 2400787 (2024).
- [47] Y. Zhang, J. Yang, Z. Chen, H. Feng, S. Zhu, K.-M. Shum, C. H. Chan, and C. Wang, *arXiv preprint arXiv:2406.19620* (2024).
- [48] R. Ding, Y. Liu, Y. Ma, Y. Yang, Q. Li, A. E.-J. Lim, G.-Q. Lo, K. Bergman, T. Baehr-Jones, and M. Hochberg, *Journal of Lightwave Technology* **32**, 2240 (2014).
- [49] D. Patel, S. Ghosh, M. Chagnon, A. Samani, V. Veerasubramanian, M. Osman, and D. V. Plant, *Optics Express* **23**, 14263 (2015).
- [50] X. Wang, W. Shen, W. Li, Y. Liu, Y. Yao, J. Du, Q. Song, and K. Xu, *Photonics Research* **9**, 535 (2021).
- [51] D. Zhuang, Q. Na, Q. Xie, N. Zhang, L. Zhang, X. Li, G. Zuo, H. Zhang, L. Wang, L. Qin, and J. Song, *IEEE Photonics Journal* **16**, 1 (2024).
- [52] H. Yu and W. Bogaerts, *Journal of Lightwave Technology* **30**, 1602 (2012).
- [53] Y. Zhou, L. Zhou, H. Zhu, C. Wong, Y. Wen, L. Liu, X. Li, and J. Chen, *Photonics Research* **4**, 153 (2016).
- [54] K. Zhu, V. Saxena, X. Wu, and W. Kuang, *IEEE Transactions on Circuits and Systems II: Express Briefs* **62**, 412 (2015).
- [55] S. Lin, S. Moazeni, K. T. Settaluri, and V. Stojanovic, *Journal of Lightwave Technology* **35**, 4766 (2017).
- [56] D. Ming, Y. Wang, Z. Wang, K. X. Wang, C. Qiu, and M. Tan, *IEEE Transactions on Circuits and Systems I: Regular Papers* **71**, 1819 (2024).
- [57] H. Bahrami, H. Sepehrian, C. S. Park, L. A. Rusch, and W. Shi, *Journal of Lightwave Technology* **34**, 2812 (2016).
- [58] Q. Zhang, J. Zhou, and J. Hong, *IEEE Photonics Technology Letters* **31**, 1072 (2019).
- [59] T. Herr, K. Hartinger, J. Riemensberger, C. Y. Wang, E. Gavartin, R. Holzwarth, M. L. Gorodetsky, and T. J. Kippenberg, *Nature Photonics* **6**, 480 (2012).
- [60] D. J. Moss, R. Morandotti, A. L. Gaeta, and M. Lipson, *Nature Photonics* **7**, 597 (2013).
- [61] I. A. Sukhoivanov and I. V. Guryev, *Photonic Crystals: Physics and Practical Modeling*, 1st ed., Springer Series in Optical Sciences, Vol. 139 (Springer, Berlin, Heidelberg, 2009) pp. XIX, 242.
- [62] P. Cheben, R. Halir, J. H. Schmid, H. A. Atwater, and D. R. Smith, *Nature* **560**, 565 (2018).
- [63] R. Soref and B. Bennett, *IEEE Journal of Quantum Electronics* **23**, 123 (1987).
- [64] R. S. Weis and T. K. Gaylord, *Applied Physics A: Solids and Surfaces* **37**, 191 (1985).
- [65] D. M. Pozar, *Microwave Engineering*, 4th ed. (John Wiley & Sons, 2011).

- [66] G. Ghione, *Semiconductor Devices for High-Speed Optoelectronics*, 1st ed. (Cambridge University Press, 2009).
- [67] Z. Zhang and S. Satpathy, *Physical Review Letters* **65**, 2650 (1990).
- [68] C. Fietz, Y. Urzhumov, and G. Shvets, *Optics Express* **19**, 19027 (2011).
- [69] S. Li, L. Cai, D. Gao, J. Dong, J. Hou, C. Yang, S. Chen, and X. Zhang, *Optics Express* **28**, 35395 (2020).
- [70] Y. Zhang, L. Shao, J. Yang, Z. Chen, K. Zhang, K.-M. Shum, D. Zhu, C. H. Chan, M. Lončar, and C. Wang, *Photonics Research* **10**, 2380 (2022).
- [71] X. Hao, L. Xianyao, X. Xi, L. Zhiyong, Y. Yude, and Y. Jinzhong, *IEEE Journal of Selected Topics in Quantum Electronics* **20**, 23 (2014).
- [72] M. Xu, W. Chen, M. He, X. Wen, Z. Ruan, J. Xu, L. Chen, L. Liu, S. Yu, and X. Cai, *APL Photonics* **4**, 100802 (2019).
- [73] D. A. Pogorelaya, A. S. Aleynik, A. N. Nikitenko, M. A. Smolovik, and V. E. Strigalev, *IEEE Sensors Journal* **19**, 8733 (2019).
- [74] M. Yu, R. Cheng, C. Reimer, L. He, K. Luke, E. Puma, L. Shao, A. Shams-Ansari, X. Ren, H. R. Grant, L. Johansson, M. Zhang, and M. Lončar, *Nature Photonics* **17**, 666 (2023).
- [75] M. Liu, X. Yin, E. Ulin-Avila, B. Geng, T. Zentgraf, L. Ju, F. Wang, and X. Zhang, *Nature* **474**, 64 (2011).
- [76] J. Liu, M. Beals, A. Pomerene, S. Bernardis, R. Sun, J. Cheng, L. C. Kimerling, and J. Michel, *Nature Photonics* **2**, 433 (2008).
- [77] T. Hiraki, T. Aihara, Y. Maeda, T. Fujii, T. Tsuchizawa, K. Takahata, T. Kakitsuka, and S. Matsuo, *Journal of Lightwave Technology* **39**, 5300 (2021).
- [78] D. Marpaung, M. Pagani, B. Morrison, and B. J. Eggleton, *Journal of Lightwave Technology* **32**, 3421 (2014).
- [79] R. Sahu, L. Qiu, W. Hease, G. Arnold, Y. Minoguchi, P. Rabl, and J. M. Fink, *Science* **380**, 718 (2023).

# Supplementary Materials for: Perspective of high-speed Mach-Zehnder modulators based on nonlinear optics and complex band structures

Shuyi Li,<sup>1,\*</sup> Wei Luo,<sup>2,\*</sup> Zhenyu Li,<sup>3,†</sup> and Junqiu Liu<sup>1,4,‡</sup>

<sup>1</sup>*International Quantum Academy, Shenzhen 518048, China*

<sup>2</sup>*Department of Electrical and Electronic Engineering,  
The Hong Kong Polytechnic University, Hong Kong, China*

<sup>3</sup>*Linkstar Microtronics Pte. Ltd., Singapore 118222, Singapore*

<sup>4</sup>*Hefei National Laboratory, University of Science and Technology of China, Hefei 230088, China*

(Dated: February 21, 2025)

## Supplementary Note 1. Temporal coupled-mode equations

In the frequency domain, for RF and optical waveguides oriented in the  $z$ -direction, Maxwell's equations are expressed as

$$\begin{cases} \nabla_t \times \mathbf{H} + \hat{z} \frac{\partial}{\partial z} \times \mathbf{H} = \sigma \mathbf{E} - i\omega \mathbf{D} \\ \nabla_t \times \mathbf{E} + \hat{z} \frac{\partial}{\partial z} \times \mathbf{E} = i\omega \mu_0 \mathbf{H} \end{cases} \quad (1)$$

where  $\mathbf{D} = \varepsilon_0 \varepsilon_r \mathbf{E} + \mathbf{P}$ . We use the effective permittivity  $\varepsilon_{re} = \varepsilon_r - \sigma / (i\omega \varepsilon_0)$  to unify metals and dielectrics. The nonlinearity  $\mathbf{P}$  in the frequency domain is expressed as a Taylor series of the electric field  $\mathbf{E}$  up to the fourth order:

$$\mathbf{P} = \varepsilon_0 \chi^{(2)} \mathbf{E} \mathbf{E} + \varepsilon_0 \chi^{(3)} \mathbf{E} \mathbf{E} \mathbf{E} + \varepsilon_0 \chi^{(4)} \mathbf{E} \mathbf{E} \mathbf{E} \mathbf{E} + \dots \quad (2)$$

where  $\chi^{(n)}$  is the  $n^{\text{th}}$ -order nonlinear coefficient. Since  $\mathbf{P}$  is small, the mode expansion is employed, with  $\mathbf{P}$  serving as the perturbation that induces modal coupling between different frequencies. Based on Eq. 1, the modes used in the mode expansion are solved from

$$\begin{cases} \nabla_t \times \mathbf{H}_{p,\omega} + i\gamma_{p,\omega} \hat{z} \times \mathbf{H}_{p,\omega} + i\omega \varepsilon_0 \varepsilon_{re} \mathbf{E}_{p,\omega} = 0 \\ \nabla_t \times \mathbf{E}_{p,\omega} + i\gamma_{p,\omega} \hat{z} \times \mathbf{E}_{p,\omega} - i\omega \mu_0 \mathbf{H}_{p,\omega} = 0 \end{cases} \quad (3)$$

where  $\mathbf{E}_{p,\omega}$  and  $\mathbf{H}_{p,\omega}$  are the  $p^{\text{th}}$ -order mode fields, and  $\gamma_{p,\omega} = i\alpha_{p,\omega} + \beta_{p,\omega}$  is the mode propagation constant at frequency  $\omega$ . The mode orthogonality condition (for  $p \neq q$ ) is

$$\iint dS \hat{z} \cdot (\mathbf{E}_{p,\omega} \times \mathbf{H}_{q,\omega}) = 0 \quad (4)$$

where the integration is performed over the cross-section of the RF or optical waveguide. For the TW-MZM, only the fundamental modes ( $p = 0$ ) are used. We save this  $p = 0$  in the following derivation.

The EM fields in the TW-MZM are assumed in superposition of several narrow frequency bands, numbered as  $m$ . The central frequency of the  $m^{\text{th}}$  band is noted as  $\omega_m$ . Within each band, the mode fields are approximately unchanged, i.e.,  $\mathbf{E}_\omega \approx \mathbf{E}_{\omega_m}$  and  $\mathbf{H}_\omega \approx \mathbf{H}_{\omega_m}$ . The  $\mathbf{E}_{\omega_m}$  and  $\mathbf{H}_{\omega_m}$  are denoted as  $\mathbf{E}_m$  and  $\mathbf{H}_m$  for simplicity. Therefore, the EM fields in the TW-MZM are

$$\begin{aligned} \mathbf{E} &= \sum_m A_{m,F}(z, t) \mathbf{E}_m(x, y) \exp(i\beta_m z - i\omega_m t) + c.c. \\ &+ \sum_m A_{m,R}(z, t) \mathbf{E}_m^R(x, y) \exp(-i\beta_m z - i\omega_m t) + c.c. \end{aligned} \quad (5)$$

$$\begin{aligned} \mathbf{H} &= \sum_m A_{m,F}(z, t) \mathbf{H}_m(x, y) \exp(i\beta_m z - i\omega_m t) + c.c. \\ &+ \sum_m A_{m,R}(z, t) \mathbf{H}_m^R(x, y) \exp(-i\beta_m z - i\omega_m t) + c.c. \end{aligned} \quad (6)$$

where  $\beta_m$  represents the phase constant at  $\omega_m$ . The  $A_{m,F}(z, t)$  and  $A_{m,R}(z, t)$  are the forward and reflected amplitudes. The  $\mathbf{E}_m^R(x, y)$  and  $\mathbf{H}_m^R(x, y)$  denote the mode fields in the reflection direction. The relations between these mode fields in the two directions are  $\mathbf{E}_m^R = E_{m,x} \hat{x} + E_{m,y} \hat{y} - E_{m,z} \hat{z}$  and  $\mathbf{H}_m^R = -H_{m,x} \hat{x} - H_{m,y} \hat{y} + H_{m,z} \hat{z}$ .

Substituting Fourier-transformed Eq. 5 and Eq. 6 with the mode orthogonality condition Eq. 4 into Eq. 1, the frequency-domain coupled mode equations in the  $m^{\text{th}}$  band are obtained as

$$\begin{cases} \left( \frac{\partial}{\partial z} + \alpha_m + i\beta_m - i\beta_\omega \right) A_{m,F}(z, \omega - \omega_m) = N_{m,F}(z, \omega) \\ \left( -\frac{\partial}{\partial z} + \alpha_m + i\beta_m - i\beta_\omega \right) A_{m,R}(z, \omega - \omega_m) = N_{m,R}(z, \omega) \end{cases} \quad (7)$$

where  $N_{m,F}(z, \omega)$  and  $N_{m,R}(z, \omega)$  are defined as

$$\begin{cases} N_{m,F}(z, \omega) = i \iint dS \mathbf{E}_m \cdot \mathbf{P} \exp(-i\beta_m z) \\ N_{m,R}(z, \omega) = i \iint dS \mathbf{E}_m \cdot \mathbf{P} \exp(i\beta_m z) \end{cases} \quad (8)$$

The integration is introduced from the mode orthogonality condition Eq. 4. Using the Taylor expansion on  $\beta_\omega$ , we can have

$$\beta_\omega - \beta_m = \beta_{1,m} (\omega - \omega_m) + \frac{1}{2} \beta_{2,m} (\omega - \omega_m)^2 + o(\omega - \omega_m)^2 \quad (9)$$

where  $\beta_{1,m}$  and  $\beta_{2,m}$  are related with the group index and its dispersion. The  $\beta_{2,m}$  can be discarded in our case. The  $\chi$  is assumed to be different constants for RF and optical waves. With Fourier transformation, the temporal coupled mode equations (TCME) are obtained as

$$\begin{cases} \left( \frac{\partial}{\partial z} + \alpha_m + \frac{1}{v_{g,m}} \frac{\partial}{\partial t} \right) A_{m,F}(z, t) = N_{m,F}(z, t) \\ \left( -\frac{\partial}{\partial z} + \alpha_m + \frac{1}{v_{g,m}} \frac{\partial}{\partial t} \right) A_{m,R}(z, t) = N_{m,R}(z, t) \end{cases} \quad (10)$$

where  $\beta_{1,m} = 1/v_{g,m}$ . And the  $N_{m,F}(z, t)$  and  $N_{m,R}(z, t)$  are

$$\begin{cases} N_{m,F}(z, t) = i \iint dS \mathbf{E}_m \cdot \mathbf{P} \exp(-i\beta_m z + i\omega_m t) \\ N_{m,R}(z, t) = i \iint dS \mathbf{E}_m \cdot \mathbf{P} \exp(i\beta_m z + i\omega_m t) \end{cases} \quad (11)$$

The derived TCMEs for a TW-MZM are consistent with the equations used in nonlinear optics<sup>1</sup>.

The EM fields in the TW-MZM involve one static electric field  $E_{dc}$  induced by the bias voltage  $V_{dc}$ , one optical wave  $E_{opt}$  with amplitude  $A_{opt}$ , and one forward RF wave with amplitude  $A_{rf,F}$ . Caused by impedance mismatch, the forward RF wave is accompanied by a reflected RF wave with amplitude  $A_{rf,R}$ . The forward and reflected RF waves share the same electric field  $E_{rf}$ . Note that  $E_{dc}$ ,  $E_{opt}$ , and  $E_{rf}$  are all dominant components of the normalized electric field distribution. The superposed electric field  $\mathbf{E}$  in the TW-MZM is expressed as

$$\begin{aligned} \mathbf{E} = & V_{dc} E_{dc}(x, y) \hat{e}_{dc} \\ & + A_{rf,F}(z, t) E_{rf}(x, y) \hat{e}_{rf} \exp(i\beta_{rf} z - i\omega_{rf} t) + c.c. \\ & + A_{rf,R}(z, t) E_{rf}(x, y) \hat{e}_{rf} \exp(-i\beta_{rf} z - i\omega_{rf} t) + c.c. \\ & + A_{opt}(z, t) E_{opt}(x, y) \hat{e}_{opt} \exp(i\beta_{opt} z - i\omega_{opt} t) + c.c. \end{aligned} \quad (12)$$

where  $\hat{e}_{dc}$ ,  $\hat{e}_{rf}$  and  $\hat{e}_{opt}$  are the dominant polarization directions for  $E_{dc}$ ,  $E_{rf}$ , and  $E_{opt}$ , respectively. Substituting Eq. 2 and Eq. 12 into Eq. 10, the TCME for  $A_{rf,F}$ ,  $A_{rf,R}$  and  $A_{opt}$  are obtained as Eq. (1a-1c) in the main manuscript.

In the case of low RF power with single-frequency  $A_{rf,F}$  (i.e.  $A_{rf,F}$  is time-independent and  $|A_{rf,F}|^2 \rightarrow 0$ ), the terms containing  $|A_{rf,F}|^2$  in Eq. 2 in the main manuscript are nullified. Thus, Eq. 1a in the main manuscript is simplified as

$$\frac{\partial}{\partial z} A_{rf,F} = (-\alpha_{rf} + i\Delta\beta_{rf}) A_{rf,F} \quad (13)$$

where  $\Delta\beta_{rf} = 2\Lambda_{dr,12} V_{dc} + 3\Lambda_{dr,22} V_{dc}^2 + 4\Lambda_{dr,32} V_{dc}^3$ . Solving Eq. 13 yields the  $\Delta n_{eff,rf}$  expression in Eq. 8b in the main manuscript.

In the case of single-frequency (continuous-wave)  $A_{opt}$  with  $V_{dc} \neq 0$ ,  $A_{rf,F} = 0$ , and  $A_{rf,R} = 0$ , Eq. 1c in the main manuscript becomes

$$\frac{\partial}{\partial z} A_{opt} = (-\alpha_{opt} + i\Delta\beta_{opt}) A_{opt} \quad (14)$$

where  $\Delta\beta_{opt} = 2\Lambda_{dr,12} V_{dc} + 3\Lambda_{dr,22} V_{dc}^2 + 4\Lambda_{dr,32} V_{dc}^3$ . Solving Eq. 14 yields the  $\Delta n_{eff,opt}$  expression in Eq. 8a in the main manuscript.

## Supplementary Note 2. Semiconductor simulation and experiment

The semiconductor simulation is based on solving several equations. Poisson's equation describes the electrostatic potential, simplified from Maxwell's equations by neglecting magnetic field. The drift-diffusion equations address the density of electrons ( $n$ ) and holes ( $p$ ), derived from the Boltzmann's equation. Additionally, various material models are applied in simulation, including mobility, band-gap narrowing, and trap-assisted recombination<sup>2,3</sup>.



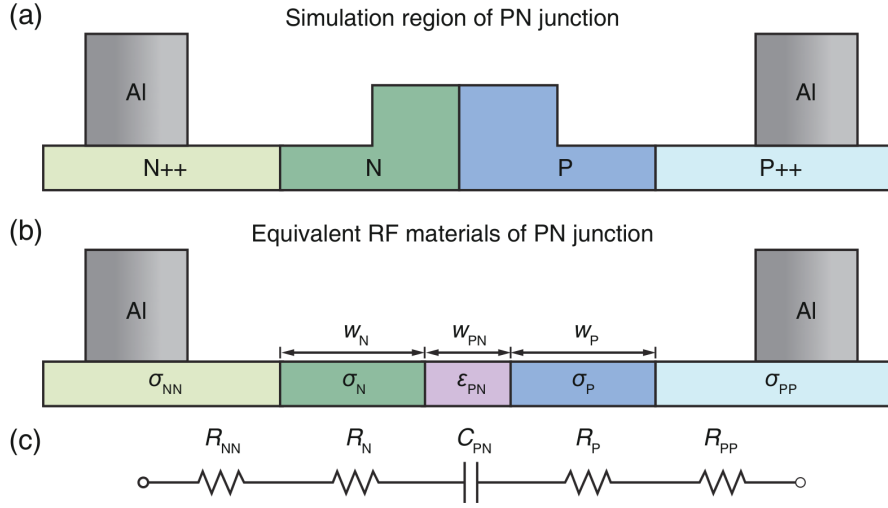


Figure S1. (a) Illustration of doping areas of the PN junction for semiconductor simulation. (b) Equivalent RF materials of the PN junction for RF mode solver. (c) Small-signal electrical circuit model of the PN junction.

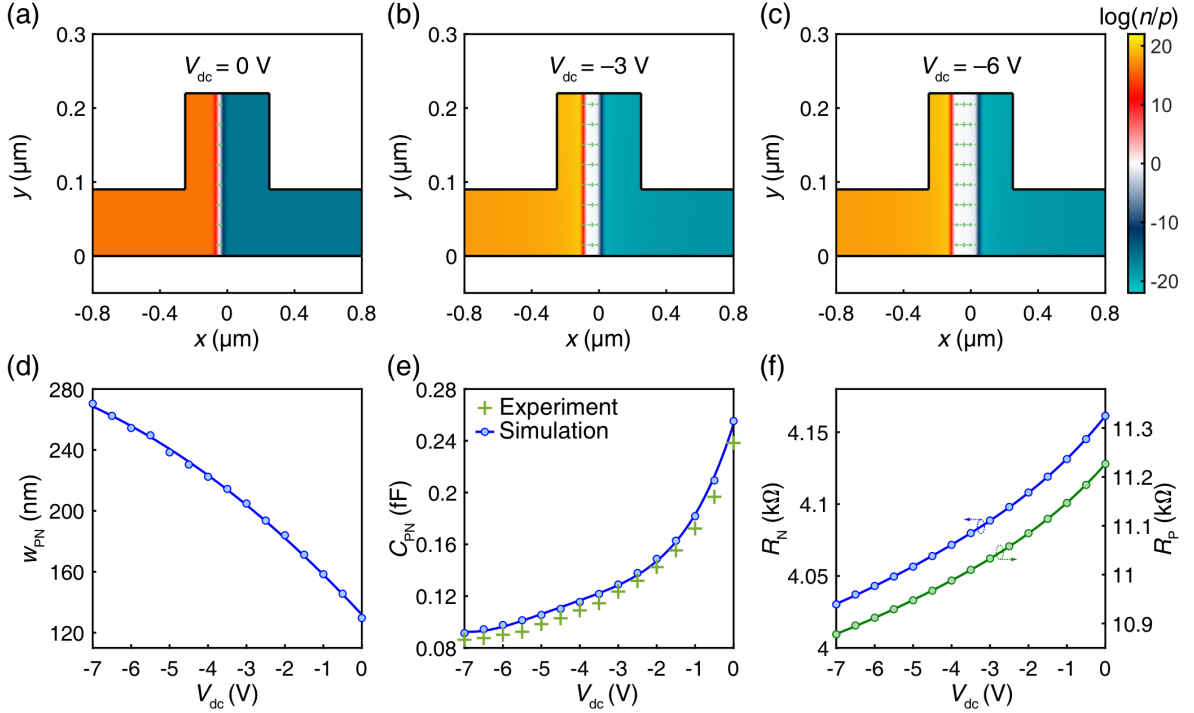


Figure S2. (a–c) Simulation results of  $\log(n/p)$  under  $V_{dc}$  of 0 V (a),  $-3$  V (b) and  $-6$  V (c). The static electric fields are illustrated as the green vector fields. (d) The  $w_{PN}$  versus  $V_{dc}$  and fit with a second-order polynomial. (e) Simulated (blue curve) and experimental (green crosses) relation of the capacitance  $C_{PN}$  versus  $V_{dc}$ . (f) Resistance  $R_N$  (left  $y$ -axis) and  $R_P$  (right  $y$ -axis) versus  $V_{dc}$ . The curves of  $C_{PN}$ ,  $R_N$  and  $R_P$  are all fitted by fourth-order polynomials, respectively.

Figure S1(a) illustrates the doping area of the PN junction in semiconductor simulation. The PN junction is positioned within an optical rib waveguide which is 500 nm wide and 220 nm high. Its slab region is 90 nm thick. The P region is slightly larger than the N region to optimize the optical effective mode index change. To minimize optical absorption loss, P++ and N++ regions are positioned 950 nm away from the waveguide. These highly doped regions form ohmic contacts with aluminium electrodes. The statistics of  $n$  and  $p$  follow the Fermi-Dirac distribution at 300 K. The carrier mobility is based on Masetti model<sup>4</sup>. The  $V_{dc}$  is swept from 0 V to  $-7$  V on the anode of the PN junction, with  $-0.5$  V increments.

The PN junction is converted to the equivalent conductivity and permittivity for RF mode solving as Fig. **S1**(b). Five regions ( $\sigma_{\text{NN}}$ ,  $\sigma_{\text{N}}$ ,  $\sigma_{\text{P}}$ ,  $\sigma_{\text{PP}}$ ,  $\epsilon_{\text{PN}}$ ) are obtained based on the small-signal electrical circuit model as Fig. **S1**(c). The  $\sigma_{\text{NN}} / \sigma_{\text{PP}}$  are determined by the square resistance  $R_{\text{NN}} / R_{\text{PP}}$  and thickness  $t_{\text{NN}} / t_{\text{PP}}$  by  $\sigma_{\text{NN,PP}} = 1 / (R_{\text{NN,PP}} t_{\text{NN,PP}})$ . The  $\sigma_{\text{N}}$ ,  $\sigma_{\text{P}}$  and  $\epsilon_{\text{PN}}$  are derived from the consumed electrical power by PN junction. The electrical power based on the electrical circuit in Fig. **S1**(c) is  $P = Z\delta I^2$  under reversed bias voltage. Meanwhile, from the EM-field perspective, the consumed electrical power is

$$\begin{aligned} P &= \iiint_{\text{PN}} dV (i\omega \mathbf{E} \cdot \epsilon_{\text{PN}} \mathbf{E}) + \iiint_{\text{N}} dV (\mathbf{E} \cdot \sigma_{\text{N}} \mathbf{E}) + \iiint_{\text{P}} dV (\mathbf{E} \cdot \sigma_{\text{P}} \mathbf{E}) \\ &= \frac{w_{\text{PN}} t_{\text{PN}} L_s}{i\omega \epsilon_{\text{PN}}} \langle \mathbf{J}_{\text{D}}^2 \rangle + \frac{w_{\text{N}} t_{\text{N}} L_s}{\sigma_{\text{N}}} \langle \mathbf{J}_{\text{N}}^2 \rangle + \frac{w_{\text{P}} t_{\text{P}} L_s}{\sigma_{\text{P}}} \langle \mathbf{J}_{\text{P}}^2 \rangle \end{aligned} \quad (15)$$

where  $\mathbf{J}_{\text{D}}$  and  $\mathbf{J}$  are the densities of displacement current and conducting current, respectively. The expressions of  $\mathbf{J}_{\text{D}}$  and  $\mathbf{J}$  are

$$\begin{cases} \mathbf{J}_{\text{D}} = i\omega \epsilon_{\text{PN}} \mathbf{E} \\ \mathbf{J}_{\text{N,P}} = \frac{1}{\sigma_{\text{N,P}}} \mathbf{E} \end{cases} \quad (16)$$

The  $\langle \rangle$  means the volume average, which is defined as:

$$\langle \rangle = \frac{1}{w_{\text{M}} t_{\text{M}} L_s} \iiint_{\text{M}} dV \quad (17)$$

The symbol M represents PN, N or P regions. The  $w_{\text{PN}}$ ,  $w_{\text{N}}$  and  $w_{\text{P}}$  are the width of  $\epsilon_{\text{PN}}$ ,  $\sigma_{\text{N}}$  and  $\sigma_{\text{P}}$  regions, respectively. The  $t_{\text{PN}}$ ,  $t_{\text{N}}$  and  $t_{\text{P}}$  denote the thickness of  $\epsilon_{\text{PN}}$ ,  $\sigma_{\text{N}}$  and  $\sigma_{\text{P}}$  regions, respectively. The  $L_s$  is set as 1  $\mu\text{m}$  in the simulation.

Assuming  $t_{\text{N}} L_s \sqrt{\langle \mathbf{J}_{\text{N}}^2 \rangle} = t_{\text{P}} L_s \sqrt{\langle \mathbf{J}_{\text{P}}^2 \rangle} = t_{\text{PN}} L_s \sqrt{\langle \mathbf{J}_{\text{D}}^2 \rangle} = \delta I$ ,  $\sigma_{\text{P}}$ ,  $\sigma_{\text{N}}$  and  $\epsilon_{\text{PN}}$  are listed as below.

$$\begin{cases} \sigma_{\text{N}} = \frac{w_{\text{N}}}{R_{\text{N}} L_s t_{\text{N}}} \\ \sigma_{\text{P}} = \frac{w_{\text{P}}}{R_{\text{P}} L_s t_{\text{P}}} \\ \epsilon_{\text{PN}} = \frac{w_{\text{PN}} C_{\text{PN}}}{L_s t_{\text{PN}}} \end{cases} \quad (18)$$

Figure **S2**(a-c) show the simulation results of  $\log(n/p)$  under  $V_{\text{dc}} = 0, -3, -6$  V, respectively. The  $x$ -component of the static electric field  $E_{\text{dc}}$  is illustrated as a green vector field in Fig. **S2**(a-c). The  $E_{\text{dc}}$  is primarily located in the depletion zone and points from the N region toward the P region.

The width of the depletion zone is  $w_{\text{PN}}$ . Figure **S2**(d) presents the curve of  $w_{\text{PN}}$  versus  $V_{\text{dc}}$  fitted by a second-order polynomial. The  $w_{\text{PN}}$  is obtained by measuring the distance of two points where  $E_{\text{dc}}$  is equal to 1% of its peak value.

The blue curve in Fig. **S2**(e) is the simulated capacitance  $C_{\text{PN}}$  varying with  $V_{\text{dc}}$ . The green crosses are the measured  $C_{\text{PN}}$  at 10 kHz using an LCR meter, which agree with the simulated  $C_{\text{PN}}$ . Figure **S2**(f) displays the curves of resistance  $R_{\text{N}}$  (left  $y$ -axis) and  $R_{\text{P}}$  (right  $y$ -axis) versus  $V_{\text{dc}}$ , respectively. The curves of  $C_{\text{PN}}$ ,  $R_{\text{N}}$  and  $R_{\text{P}}$  are all fitted by fourth-order polynomials, respectively.

### Supplementary Note 3. Optical simulation and experiment

The  $n_{\text{eff,opt}}$  of the Si and LiNbO<sub>3</sub> optical waveguides are obtained by solving Eq. 3. The change of Si refractive indexes ( $\Delta n_{\text{Si}}$  and  $\Delta \alpha_{\text{Si}}$ ) caused by  $V_{\text{dc}}$  are determined by Soref and Bennett's equations<sup>5</sup>.

$$\begin{cases} \Delta n_{\text{Si}} = -8.8 \times 10^{-22} n - 8.5 \times 10^{-18} p^{0.8} \\ \Delta \alpha_{\text{Si}} = 8.5 \times 10^{-18} n + 6.0 \times 10^{-18} p \end{cases} \quad (19)$$

The change of LiNbO<sub>3</sub> anisotropic refractive indexes ( $n_{\text{LN,x}}$ ,  $n_{\text{LN,y}}$  and  $n_{\text{LN,z}}$ ) are caused by the Pockels effect<sup>6</sup>.

$$\begin{cases} n_{\text{LN,x}} = n_{\text{e}} - \frac{n_{\text{e}}^3}{2} r_{33} E_{\text{dc}} \\ n_{\text{LN,y}} = n_{\text{o}} - \frac{n_{\text{o}}^3}{2} r_{13} E_{\text{dc}} \\ n_{\text{LN,z}} = n_{\text{o}} - \frac{n_{\text{o}}^3}{2} r_{13} E_{\text{dc}} \end{cases} \quad (20)$$

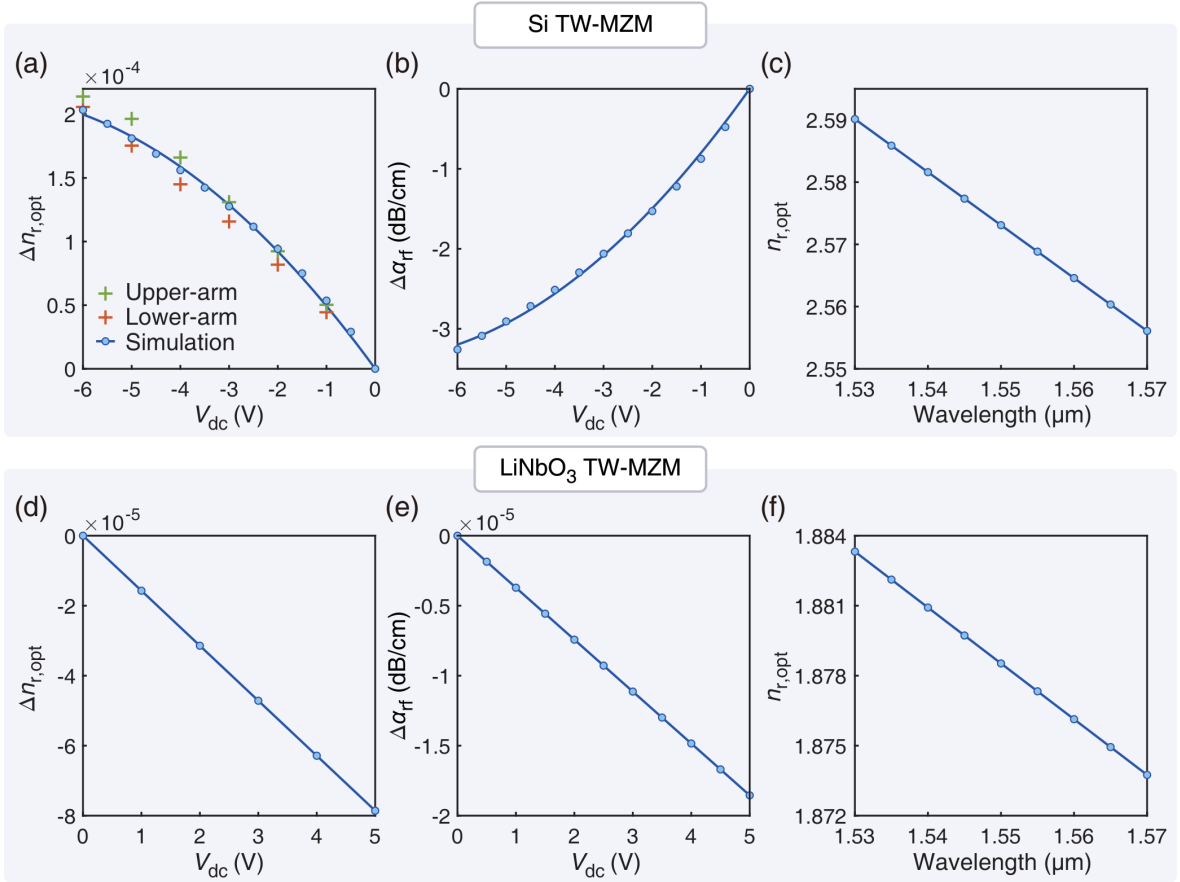


Figure S3. (a–c) and (d–f) depict the simulation results for the Si and LiNbO<sub>3</sub> TW-MZM, respectively. The  $\Delta n_{r,\text{opt}}$  (a,d) and  $\Delta\alpha_{r,\text{opt}}$  (b,e) at 1550 nm wavelength are marked with blue dots and fitted with second-order polynomials. The orange and green crosses in (a) are experimental data of  $\Delta n_{r,\text{opt}}$  on the upper and lower arms of the Si TW-MZM. (c,f) The  $n_{r,\text{opt}}$  curves with 1530 to 1570 nm wavelength.

where the  $x$ ,  $y$  and  $z$  are crystal directions of the LiNbO<sub>3</sub>. The  $n_e$  and  $n_o$  represent the extraordinary and ordinary indexes of LiNbO<sub>3</sub>, respectively. The  $r_{33}$  and  $r_{13}$  are the Pockels coefficients. The  $E_{\text{dc}}$  is obtained by solving the Poisson's equation, following the simulation process in Ref. [7].

The commercial software COMSOL is used to solve  $n_{\text{eff,opt}}$  under different  $V_{\text{dc}}$ . Figures S3 (a–f) show the simulation results ( $\Delta n_{r,\text{opt}}$ ,  $\Delta\alpha_{r,\text{opt}}$  and  $n_{r,\text{opt}}$ ) of Si and LiNbO<sub>3</sub> optical waveguides at the wavelength of 1550 nm, respectively. The  $\Delta n_{r,\text{opt}}$  in Fig. S3 (a,d) and  $\Delta\alpha_{r,\text{opt}}$  in Fig. S3 (b,e) are the changes by  $V_{\text{dc}}$ , marked as blue dots. These data are fitted by second-order polynomials to calculate  $\Lambda_{\text{dp},12}$  and  $\Lambda_{\text{dp},22}$ . The orange and green crosses in Fig. S3(a) are the measured  $\Delta n_{r,\text{opt}}$  from the upper and lower arms of the Si TW-MZM. The agreement between experimental and the simulation results validates our simulation method.

Figure S3(c,f) displays  $n_{r,\text{opt}}$  varying with optical wavelength from 1530 to 1570 nm. The  $n_{r,\text{opt}}$  is linearly changed with  $\omega_{\text{opt}}$  for both the Si and LiNbO<sub>3</sub> optical waveguide, which supports the assumption of  $\beta_{2,\text{opt}} \approx 0$  in Note 1. By linear fit, the group index is obtained as  $n_{g,\text{opt}} = 3.89$  for Si and  $n_{g,\text{opt}} = 2.25$  for LiNbO<sub>3</sub>.

Figure S4 (a,b) shows the measured transmission spectra of the Si TW-MZM when tuning the upper or the lower arm of the Si TW-MZM. The  $V_{\text{dc}}$  is swept from  $-6$  to  $0$  V in 1 V increment. The measured  $\Delta n_{r,\text{opt}}$  is calculated from the peak movement on the transmission spectra under various  $V_{\text{dc}}$ .

#### Supplementary Note 4. RF simulation with complex band structures

The  $n_{\text{eff,rf}}$  is obtained by solving the vector wave-equation with Bloch's conditions. The vector wave-equation derived from Maxwell equation Eq. 1 is Eq. 9 in the main manuscript. By dot multiplying a test function  $\mathbf{F}$  and integrating

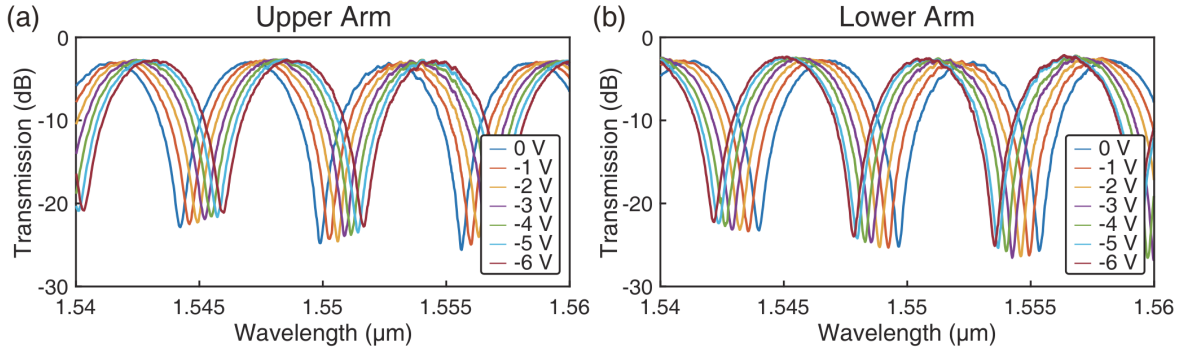


Figure S4. Measured transmission spectra of the Si TW-MZM by individually tuning  $V_{dc}$  on the PN junctions in the upper (a) or the lower (b) arms of the Si TW-MZM.

over the entire simulation region<sup>8,9</sup>, a volume integral is obtained as

$$\iiint dV \mathbf{F} \cdot (\nabla \times (\nabla \times \mathbf{E})) - k_{0,\text{rf}}^2 \mathbf{F} \cdot \varepsilon_{\text{re}} \mathbf{E} = 0 \quad (21)$$

To reduce the order of the derivative, Eq. 21 is simplified by Gauss' theorem as

$$\iiint dV (\nabla \times \mathbf{F}) \cdot (\nabla \times \mathbf{E}) - k_{0,\text{rf}}^2 \mathbf{F} \cdot \varepsilon_{\text{re}} \mathbf{E} - i\omega\mu_0 \iint dS \mathbf{F} \cdot (\hat{n}_s \times \mathbf{H}) = 0 \quad (22)$$

Based on Bloch's theorem, the EM fields are expressed as

$$\begin{cases} \mathbf{E} = \mathbf{u} \exp(i\mathbf{k} \cdot \mathbf{r}) \\ \mathbf{H} = \mathbf{v} \exp(i\mathbf{k} \cdot \mathbf{r}) \\ \mathbf{F} = \mathbf{w} \exp(-i\mathbf{k} \cdot \mathbf{r}) \end{cases} \quad (23)$$

where  $\mathbf{u}$ ,  $\mathbf{v}$  and  $\mathbf{w}$  are the Bloch mode fields. The  $\mathbf{u}$ ,  $\mathbf{v}$  and  $\mathbf{w}$  satisfy periodic boundary condition, e.g.  $\mathbf{u}(\mathbf{r} + \mathbf{R}) = \mathbf{u}(\mathbf{r})$  where  $\mathbf{R}$  represents the lattice vector. The  $\mathbf{k}$  is the Bloch wave vector. By substituting the Eq. 23 into Eq. 22, the weak form to calculate the complex band structures (CBS) is

$$\iiint dV ((\nabla - i\mathbf{k}) \times \mathbf{w}) \cdot ((\nabla + i\mathbf{k}) \times \mathbf{u}) - k_{0,\text{rf}}^2 \mathbf{w} \cdot \varepsilon_{\text{re}} \mathbf{u} - i\omega\mu_0 \iint dS \mathbf{w} \cdot (\hat{n}_s \times \mathbf{v}) = 0 \quad (24)$$

Due to the periodicity of  $\mathbf{v}$  and  $\mathbf{w}$ , the surface integral in Eq. 24 is vanished. To remain the surface integral zero in numerical simulation, the meshes on the periodic boundaries are set as copied face<sup>9</sup>.

The PN junction and LiNbO<sub>3</sub> are both thinner than the electrodes, resulting in a fine mesh grid in the simulation. To further save computational resource, the weak form in thin layer area (PN junction or LiNbO<sub>3</sub>) is converted to weak contributions. Assuming  $\mathbf{u}$  is unchanged along the thickness direction ( $y$ -direction of the unit cell), the term containing  $\varepsilon_{\text{re}}$  in Eq. 24 is simplified as

$$\iiint_{\Omega} dV \mathbf{w} \cdot \varepsilon_{\text{re}} \mathbf{u} = \iint_S dx dz \mathbf{w} \cdot (\varepsilon_{\text{re}} - \varepsilon_{\text{clad}}) t(x, z) \mathbf{u} + \iiint_{\Omega} dV \mathbf{w} \cdot \varepsilon_{\text{clad}} \mathbf{u} \quad (25)$$

where  $\Omega$  denotes the thin layer area and  $S$  represents its bottom surface for replacing the thin layer area. The  $t(x, z)$  is the thickness of the thin layer area  $\Omega$ .

The Bloch wave vectors of Si and LiNbO<sub>3</sub> electrodes' unit cells are  $\mathbf{k} = k_z \hat{z}$ . Figure S5 displays the CBS of Si (a) and LiNbO<sub>3</sub> (b) TW-MZMs in the unit of  $2\pi/L_z$ . The real and imaginary parts of  $k_z$  are illustrated in blue and green curves, respectively.

Figure S6(a-c) shows the profiles of  $n_{\text{r,rf}}$  (a),  $\alpha_{\text{rf}}$  (b), and  $Z_c$  (c) for the Si TW-MZM, with  $V_{dc}$  from 0 to -6 V and  $\omega_{\text{rf}}/2\pi$  from 10 to 120 GHz. The black dashed lines represent the contour curves of  $n_{\text{r,rf}}$ ,  $\alpha_{\text{rf}}$  and  $Z_c$ .

Figure S7 illustrates the EM fields on the cross-section at  $L_z = 0 \mu\text{m}$  of the Si (a,b) and LiNbO<sub>3</sub> (c,d) TW-MZM, respectively. The  $H_x$  and  $H_y$  in Fig. S7(a,c) are visualized as green vector fields. The electric field  $E_x$  in Fig. S7(b,d) is depicted as a hot-colored profile, normalized by the maximum field value.

For our fabricated Si TW-MZM, the T-shaped electrode's dimension is  $(L_1, L_2, g_1, g_2, w_1, w_2) = (47, 3, 6.3, 9.2, 10, 60) \mu\text{m}$ . The coefficients used for eye diagram simulation are summarized in Table S1.

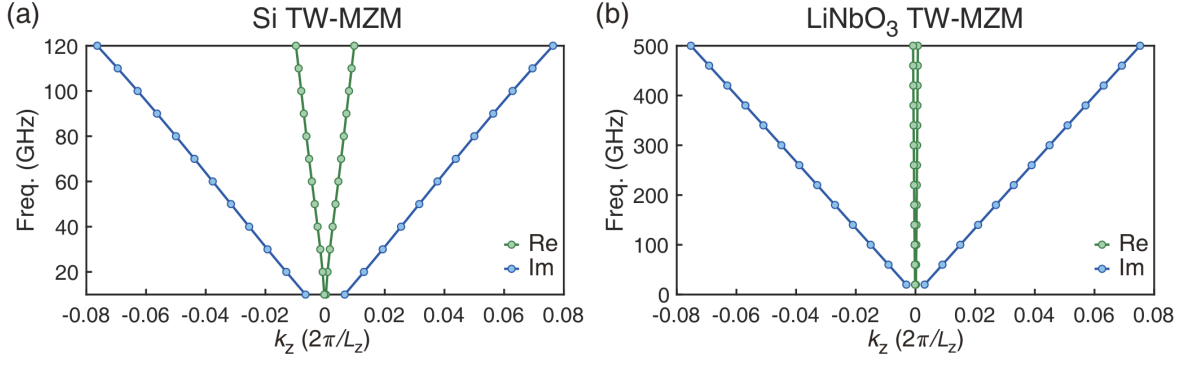


Figure S5. Complex band structures of periodic T-shaped electrodes for Si (a) and LiNbO<sub>3</sub> (b) TW-MZMs in the unit of  $2\pi/L_z$ . The blue and green curves represent the real and imaginary parts of  $k_z$ , respectively.

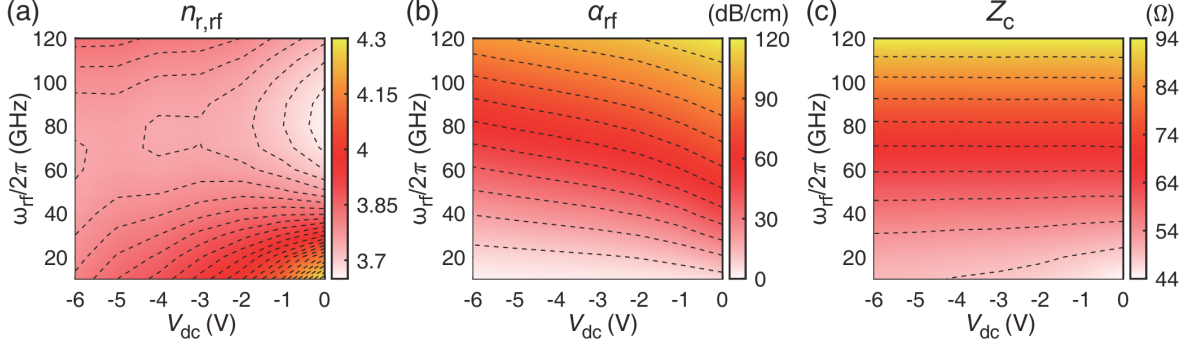


Figure S6. (a–c) Profiles of  $n_{r,rf}$ (a),  $\alpha_{rf}$ (b), and  $Z_c$ (c) of the periodic T-shaped electrodes for Si TW-MZMs. Black dashed lines represent the contours of  $n_{r,rf}$ ,  $\alpha_{rf}$  and  $Z_c$ .

Table S1. Parameters of fabricated Si TW-MZM at  $V_{dc} = -3$  V

| Symbol            | Value (@ 20 GHz)   | Symbol            | Value (@ 1550 nm)  |
|-------------------|--------------------|-------------------|--------------------|
| $\Lambda_{dr,12}$ | $33.361 + 40.211i$ | $\Lambda_{dp,12}$ | $-97.163 + 4.465i$ |
| $\Lambda_{dr,22}$ | $3.260 + 4.963i$   | $\Lambda_{dp,22}$ | $-3.331 + 0.157i$  |
| $\Lambda_{dr,32}$ | $0.146 + 0.245i$   |                   |                    |
| $n_{r,rf}$        | 3.624              | $n_{r,opt}$       | 2.573              |
| $\alpha_{rf}$     | 11.139 dB/cm       | $\alpha_{opt}$    | 5.977 dB/cm        |
| $n_{g,rf}$        | 3.266              | $n_{g,opt}$       | 3.893              |
| $Z_c$             | 60.599 $\Omega$    |                   |                    |

## Supplementary Note 5. Boundary conditions for RF TCME

The boundary conditions to solve Eq. (1a, 1b) in the main manuscript are established based on the reflection and transmission at the interface of the RF waveguide with impedance  $Z_c$ . Figure S8(a) shows the schematic of the RF input port using an RF probe in the experiment. Figure S8(b) represents the equivalent RF circuit of Fig. S8(a), where the RF waveguide is connected to a source with an inner resistor  $R_g$ . Figure S8(c) presents the schematic of the on-chip resistor functioning as an RF absorber. The equivalent RF circuit in Fig. S8(d) shows the RF waveguide connected to a load resistor  $R_L$ . Based on transmission line theory<sup>10</sup>, the complex voltage along the RF electrode is

$$\tilde{V}_{rf}(z, \omega_{rf}) = \tilde{V}_{rf,F}(z, \omega_{rf}) + \tilde{V}_{rf,R}(z, \omega_{rf}) \quad (26)$$

and the corresponding complex current is

$$\tilde{I}_{rf}(z, \omega_{rf}) = \frac{1}{Z_c} \tilde{V}_{rf,F}(z, \omega_{rf}) - \frac{1}{Z_c} \tilde{V}_{rf,R}(z, \omega_{rf}) \quad (27)$$

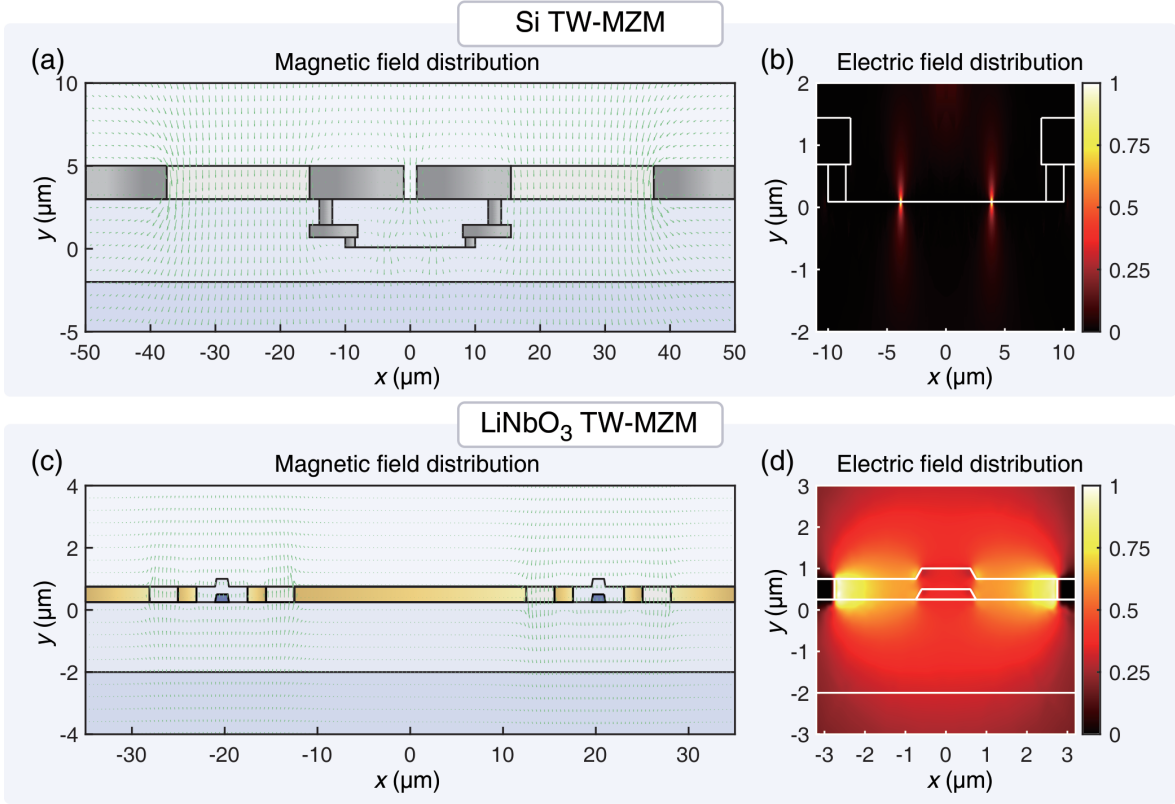


Figure S7. (a,b) and (c,d) illustrate the simulated distributions of magnetic and electric fields on the cross-section at  $L_z = 0$   $\mu\text{m}$  for the Si and  $\text{LiNbO}_3$  TW-MZM, respectively. The magnetic field distributions  $H_x$  and  $H_y$  in (a,c) are visualized as green vector fields. The electric field distributions  $E_x$  in (b,d) are depicted as a hot-color profile normalized by the maximum field value.

At the RF input port and absorber, the complex voltages are

$$\begin{cases} \tilde{V}_{\text{rf}}(0, \omega_{\text{rf}}) = \tilde{V}_{\text{in}}(\omega_{\text{rf}}) + R_g \tilde{I}_{\text{rf}}(0, \omega_{\text{rf}}) \\ \tilde{V}_{\text{rf}}(L, \omega_{\text{rf}}) = R_L \tilde{I}_{\text{rf}}(L, \omega_{\text{rf}}) \end{cases} \quad (28)$$

The  $\tilde{V}_{\text{in}} = V_{\text{in}}/2$  is based on the definition of measurable voltage in our model. We define the measurable voltage  $V = \tilde{V} + \tilde{V}^*$  following the nonlinear optics theory<sup>11</sup>, which is different from the  $V = \text{Re}(\tilde{V})$  used in Ref. [10]. Therefore, the RF boundary conditions are derived as

$$\begin{cases} \tilde{V}_{\text{rf,R}}(L, \omega_{\text{rf}}) = \Gamma_L \tilde{V}_{\text{rf,F}}(L, \omega_{\text{rf}}) \\ \tilde{V}_{\text{rf,F}}(0, \omega_{\text{rf}}) = \Gamma_g \tilde{V}_{\text{rf,R}}(0, \omega_{\text{rf}}) + \frac{1}{2} \frac{Z_c}{R_g + Z_c} V_{\text{in}}(\omega_{\text{rf}}) \end{cases} \quad (29)$$

where  $\Gamma_L$  and  $\Gamma_g$  are defined as

$$\begin{cases} \Gamma_L = \frac{R_L - Z_c}{R_L + Z_c} \\ \Gamma_g = \frac{R_g - Z_c}{R_g + Z_c} \end{cases} \quad (30)$$

We assume that  $Z_c$ ,  $R_L$  and  $R_g$  are independent with  $\omega_{\text{rf}}$ . Using Fourier transformation on Eq. 29, the RF boundary conditions in the time domain are

$$\begin{cases} \tilde{V}_{\text{rf,R}}(L, t) = \Gamma_L \tilde{V}_{\text{rf,F}}(L, t) \\ \tilde{V}_{\text{rf,F}}(0, t) = \Gamma_g \tilde{V}_{\text{rf,R}}(0, t) + \frac{1}{2} \frac{Z_c}{R_g + Z_c} V_{\text{in}}(t) \end{cases} \quad (31)$$

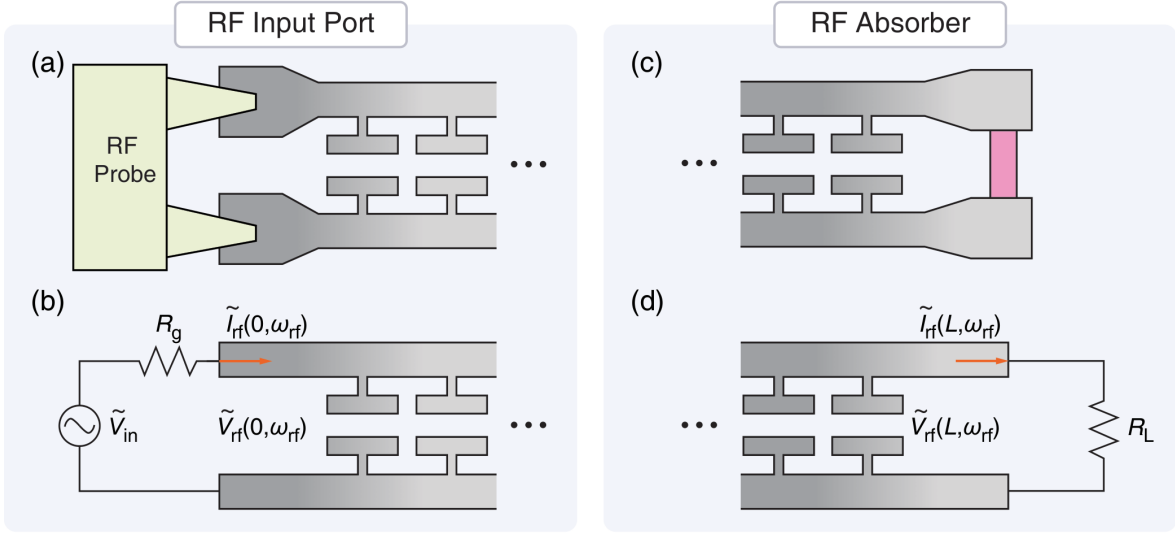


Figure S8. (a) Schematic of the RF input port using an RF probe in the experiment. (b) The equivalent RF circuit to (a). (c) Schematic of the on-chip resistor functioning as an RF absorber in the experiment. (d) The equivalent RF circuit to (c).

The relations between  $\tilde{V}_{rf,F}$  and  $A_{rf,F}$ , and between  $\tilde{V}_{rf,R}$  and  $A_{rf,R}$ , are given by

$$\begin{cases} \tilde{V}_{rf,F}(z, t) = A_{rf,F}(z, t) \exp(i\beta_{rf}z - i\omega_{rf}t) \\ \tilde{V}_{rf,R}(z, t) = A_{rf,R}(z, t) \exp(-i\beta_{rf}z - i\omega_{rf}t) \end{cases} \quad (32)$$

Therefore, the RF boundary conditions of  $A_{rf,F}$  and  $A_{rf,R}$  are

$$\begin{cases} A_{rf,R}(L, t) = \Gamma_L A_{rf,F}(L, t) \exp(2i\beta_{rf}L) \\ A_{rf,F}(0, t) = \Gamma_g A_{rf,R}(0, t) + \frac{1}{2} \frac{Z_c}{R_g + Z_c} V_{in}(t) \exp(i\omega_{rf}t) \end{cases} \quad (33)$$

## Supplementary Note 6. Numerical algorithm for solving RF and Optical TCME

The differential forms of Eq. (1a, 1b) in the main manuscript are:

$$\begin{aligned} A_{rf,F}(z + \Delta z_{rf}, t + \Delta t) &= A_{rf,F}(z, t) - \alpha_{rf} \Delta z_{rf} A_{rf,F}(z, t) \\ &+ 2i\Lambda_{dr,12} V_{dc} \Delta z_{rf} A_{rf,F}(z, t) + 3i\Lambda_{r,4} \Delta z_{rf} |A_{rf,F}(z, t)|^2 A_{rf,F}(z, t) \\ &+ 3i\Lambda_{dr,22} V_{dc}^2 \Delta z_{rf} A_{rf,F}(z, t) + 4i\Lambda_{dr,32} V_{dc}^3 \Delta z_{rf} A_{rf,F}(z, t) \\ &+ 12i\Lambda_{dr,14} V_{dc} \Delta z_{rf} |A_{rf,F}(z, t)|^2 A_{rf,F}(z, t) \end{aligned} \quad (34)$$

$$\begin{aligned} A_{rf,R}(z - \Delta z_{rf}, t + \Delta t) &= A_{rf,R}(z, t) - \alpha_{rf} \Delta z_{rf} A_{rf,R}(z, t) \\ &+ 2i\Lambda_{dr,12} V_{dc} \Delta z_{rf} A_{rf,R}(z, t) + 3i\Lambda_{r,4} \Delta z_{rf} |A_{rf,R}(z, t)|^2 A_{rf,R}(z, t) \\ &+ 3i\Lambda_{dr,22} V_{dc}^2 \Delta z_{rf} A_{rf,R}(z, t) + 6i\Lambda_{rf,4} \Delta z_{rf} |A_{rf,F}(z, t)|^2 A_{rf,R}(z, t) \\ &+ 4i\Lambda_{dr,32} V_{dc}^3 \Delta z_{rf} A_{rf,R}(z, t) \\ &+ 12i\Lambda_{dr,14} V_{dc} \Delta z_{rf} |A_{rf,R}(z, t)|^2 A_{rf,R}(z, t) \\ &+ 24i\Lambda_{dr,14} V_{dc} \Delta z_{rf} |A_{rf,F}(z, t)|^2 A_{rf,R}(z, t) \end{aligned} \quad (35)$$

The differential forms of Eq. (1c) in the main manuscript are expressed in the exponential form to release the need for a finer mesh grid size, as

$$\begin{cases} A_{opt,1}(z + \Delta z_{opt}, t + \Delta t) = \exp(\Delta\phi_1(z, t)) A_{opt,1}(z, t) \\ A_{opt,2}(z + \Delta z_{opt}, t + \Delta t) = \exp(\Delta\phi_2(z, t)) A_{opt,2}(z, t) \end{cases} \quad (36)$$

where  $\Delta\phi_1(z, t)$  and  $\Delta\phi_2(z, t)$  are defined as

$$\left\{ \begin{array}{l} \Delta\phi_1(z, t) = -\alpha_{\text{opt}}\Delta z_{\text{opt}} \\ \quad + 2i\Lambda_{\text{dp},12} (V_{\text{rf},\text{F}}(z, t) + V_{\text{rf},\text{R}}(z, t) + V_{\text{dc}}) \Delta z_{\text{opt}} \\ \quad + 3i\Lambda_{\text{dp},22} (V_{\text{rf},\text{F}}(z, t) + V_{\text{rf},\text{R}}(z, t) + V_{\text{dc}})^2 \Delta z_{\text{opt}} \\ \Delta\phi_2(z, t) = -\alpha_{\text{opt}}\Delta z_{\text{opt}} \\ \quad + 2i\Lambda_{\text{dp},12} (-V_{\text{rf},\text{F}}(z, t) - V_{\text{rf},\text{R}}(z, t) + V_{\text{dc}}) \Delta z_{\text{opt}} \\ \quad + 3i\Lambda_{\text{dp},22} (-V_{\text{rf},\text{F}}(z, t) - V_{\text{rf},\text{R}}(z, t) + V_{\text{dc}})^2 \Delta z_{\text{opt}} \end{array} \right. \quad (37)$$

The optical circuit of the TW-MZM is analysed by transfer matrix method. The transfer matrix of MMI is

$$M_{\text{MMI}} = \begin{bmatrix} \frac{1}{\sqrt{2}} & -\frac{i}{\sqrt{2}} \\ -\frac{i}{\sqrt{2}} & \frac{1}{\sqrt{2}} \end{bmatrix} \quad (38)$$

Thus the initial values of  $A_{\text{opt},1}$  and  $A_{\text{opt},2}$  are calculated by

$$\begin{bmatrix} A_{\text{opt},1}(0, t) \\ A_{\text{opt},2}(0, t) \end{bmatrix} = M_{\text{MMI}} \begin{bmatrix} 1 \\ 0 \end{bmatrix} \quad (39)$$

Therefore, the initial conditions are  $A_{\text{opt},1}(0, t) = \frac{1}{\sqrt{2}}$  and  $A_{\text{opt},2}(0, t) = -\frac{i}{\sqrt{2}}$ . Based on Eq. 36, the output of  $A_{\text{opt},1}$  and  $A_{\text{opt},2}$  can be calculated numerically. Then an additional  $\pi/2$  phase shift is added to  $A_{\text{opt},2}$  due to the 3-dB operating point. The output of the TW-MZM is  $A_{\text{opt},\text{out}}$ , which is calculated by

$$\begin{bmatrix} A_{\text{opt},\text{out}}(t) \\ A_{\text{opt},\text{drop}}(t) \end{bmatrix} = M_{\text{MMI}} \begin{bmatrix} A_{\text{opt},1}(L, t + \beta_{1,\text{opt}}L) \\ iA_{\text{opt},2}(L, t + \beta_{1,\text{opt}}L) \end{bmatrix} \quad (40)$$

## Supplementary Note 7. Algorithms Comparison

Our method offers significant improvements in efficiency and accuracy for electrode design and optoelectronic co-simulation compared to conventional methods. We provide a detailed comparison of algorithms in two aspects: simulation accuracy and efficiency.

On simulation accuracy, we compare conventional methods with our approach in Tables S2 and S3. As is evidenced, our CBS and TCME methods have naturally included many critical features of materials and structures, which are not involved in conventional methods using closed form<sup>12</sup>,  $S$ -parameter<sup>2,13-19</sup>, segmented circuit<sup>20-22</sup> and transmission-line circuit (TLC)<sup>23,24</sup>. With these critical features and properties involved, our method shows clear improvement in simulation accuracy.

On simulation efficiency, we compare conventional methods with our approach in Tables S4 and S5, demonstrating improved efficiency in our method. As is evidenced, our CBS and TCME methods have fewer restrictions compared to conventional methods that rely on  $S$ -parameters and TLC. By eliminating these restrictions and significantly reducing the simulation-region dimensions, our method achieves a clear improvement in simulation efficiency.

Figure S9(a) compares our CBS method with the  $S$ -parameter method for designing T-shaped RF electrodes in Si TW-MZMs. The  $S$ -parameter method requires additional steps, including extracting  $S$ -parameters for the electrode and multiplying T-matrices for the PN-junction-loaded circuit model. It also necessitates simulating long electrodes (e.g., 50-unit cells in Ref. [19]). In contrast, our CBS method simulates only half of a unit cell, achieving up to 100-times faster simulation speed.

Figure S9(b) compares our TCME method with the TLC method. The nonlinear RF I-V equations in the TLC method incorporate additional PN junction equations. The dispersion of the electrode is addressed by using convolution, with a computational complexity of  $O(MN)$  (where  $N$  is time steps and  $M$  is digital filters). In contrast, our method eliminates the need for convolution, reducing the computational complexity to  $O(N)$ . For example, with  $M = 16$  (as in Ref. [24]), our method is 16-times faster.

These comparisons evidence that our approach has improved efficiency and accuracy over conventional methods, marking clear advantages in design and simulation of TW-MZMs.



Table S2. Features should be included to improve accuracy of electrode simulation.

| Features   | Closed form   | $S$ -parameter | Our CBS method |
|--|---------------|----------------|----------------|
| Nonlinearity from PN junctions?                            | Not supported | Supported      | Supported      |
| Complex electrode geometry?                                | Not supported | Supported      | Supported      |
| Skin effect of electrodes?                                 | Not included  | Included       | Included       |
| Parasitic capacitance between PN junctions and electrodes? | Not included  | Not included   | Included       |

Table S3. Features should be included to improve accuracy of optoelectronic co-simulation.

| Features                        | Segmented circuit | TLC       | Our TCME method |
|---------------------------------|-------------------|-----------|-----------------|
| RF wave propagation?            | Not supported     | Supported | Supported       |
| Optical wave propagation?       | Not supported     | Supported | Supported       |
| Electrode dispersion?           | Not supported     | Supported | Supported       |
| Nonlinearity from PN junctions? | Supported         | Supported | Supported       |

Table S4. Steps in electrode simulation.

| Steps                        | $S$ -parameter | Our CBS method |
|------------------------------|----------------|----------------|
| Semiconductor simulation?    | Required       | Required       |
| Simulation-region dimension? | 50-unit cells  | 1/2-unit cells |
| $S$ -parameter extraction?   | Required       | Not needed     |
| Multiplying T-matrices?      | Required       | Not needed     |

Table S5. Steps in optoelectronic co-simulation.

| Steps                                | TLC      | Our TCME method |
|--------------------------------------|----------|-----------------|
| Additional equation for PN junction? | Required | Not needed      |
| Equivalent dispersion component?     | Required | Not needed      |
| Convolution calculation?             | Required | Not needed      |
| Solving optical equation?            | Required | Required        |

## Supplementary Note 8. Comparison between Simulation and Experimental Results

Our electrode simulation results up to 500 GHz are validated by the experimental data reported in Ref. [19]. The  $\alpha_{\text{rf}} = 2$  dB/mm at 500 GHz in Ref. [19] aligns well with our simulated  $\alpha_{\text{rf}} = 19$  dB/cm. The measured  $S_{21}$  parameters were fitted using the empirical equation:  $S_{21} = (\alpha_c \sqrt{f} + \alpha_d f)L + A$ , with  $\alpha_c = 0.264$  dB cm $^{-1}$  GHz $^{-1/2}$  and  $\alpha_d = 0.028$  dB cm $^{-1}$  GHz $^{-1}$ . Our simulations conducted over the 2 ~ 500 GHz yield comparable coefficients of  $\alpha_c = 0.338$  dB cm $^{-1}$  GHz $^{-1/2}$  and  $\alpha_d = 0.022$  dB cm $^{-1}$  GHz $^{-1}$ . Fig. S10 illustrates the agreement between the simulated  $\alpha_{\text{rf}}$  with the measurements. The slightly higher measured  $\alpha_{\text{rf}}$  at high frequency are primarily attributed to surface roughness and structural imperfections in the fabricated devices.

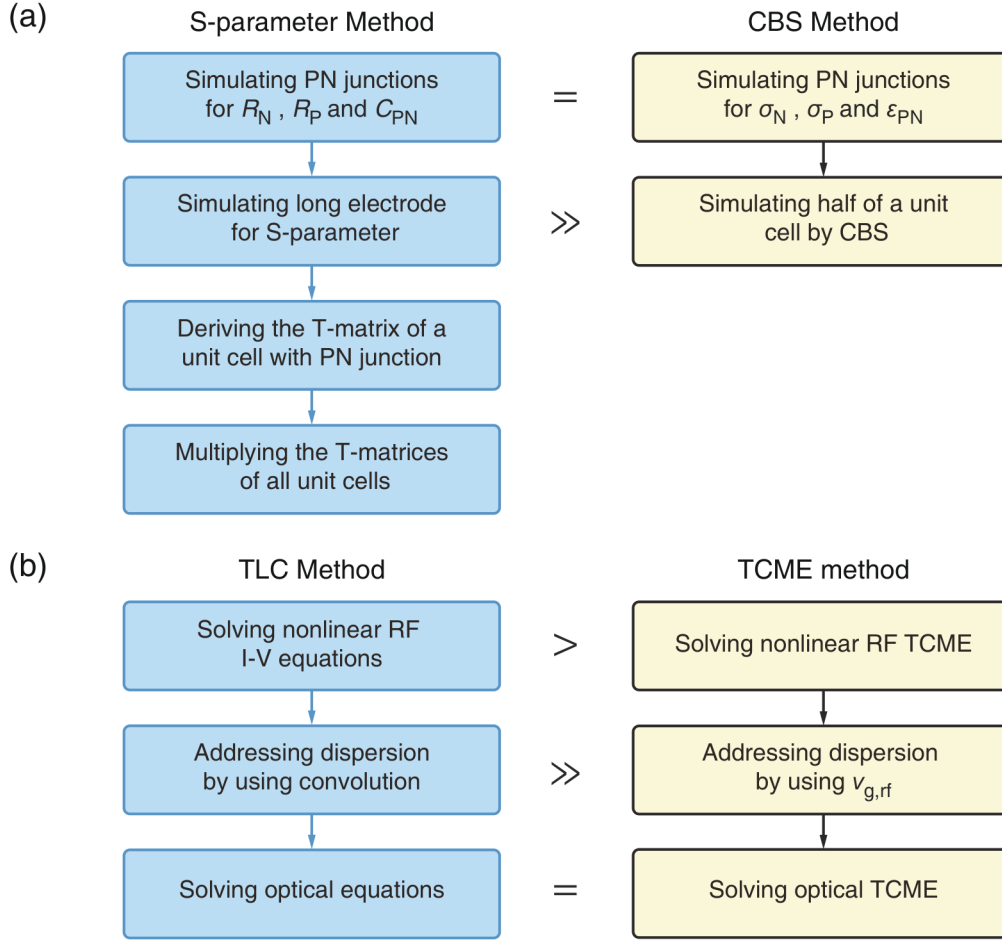


Figure S9. Comparison of algorithms for electrode design (a) and opto-electronics co-simulation (b) of Si TW-MZM.

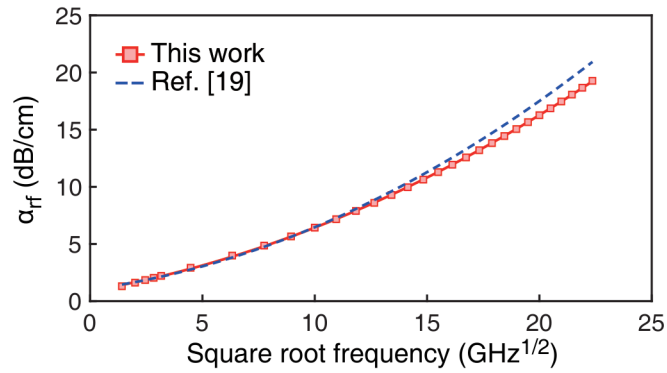


Figure S10. Comparison of the  $\alpha_{rf}$  between our simulation results and experimental data from Ref. [19].

- 
- \* These authors contributed equally to this work.
- † Contact author: [ray.shower19@gmail.com](mailto:ray.shower19@gmail.com)
- ‡ Contact author: [liujq@iqasz.cn](mailto:liujq@iqasz.cn)
- <sup>1</sup> S. Coen, H. G. Randle, T. Sylvestre, and M. Erkintalo, *Optics Letters* **38**, 37 (2013).
  - <sup>2</sup> D. Patel, S. Ghosh, M. Chagnon, A. Samani, V. Veerasubramanian, M. Osman, and D. V. Plant, *Optics Express* **23**, 14263 (2015).
  - <sup>3</sup> S. T. Lim, *Frontiers in Physics* **3** (2015), 10.3389/fphy.2015.00027.
  - <sup>4</sup> G. Masetti, M. Severi, and S. Solmi, *IEEE Transactions on Electron Devices* **30**, 764 (1983).
  - <sup>5</sup> R. Soref and B. Bennett, *IEEE Journal of Quantum Electronics* **23**, 123 (1987).
  - <sup>6</sup> R. S. Weis and T. K. Gaylord, *Applied Physics A: Solids and Surfaces* **37**, 191 (1985).
  - <sup>7</sup> Y. Liu, H. Li, J. Liu, S. Tan, Q. Lu, and W. Guo, *Optics Express* **29**, 6320 (2021).
  - <sup>8</sup> C. Fietz, Y. Urzhumov, and G. Shvets, *Optics Express* **19**, 19027 (2011).
  - <sup>9</sup> S. Li, L. Cai, D. Gao, J. Dong, J. Hou, C. Yang, S. Chen, and X. Zhang, *Optics Express* **28**, 35395 (2020).
  - <sup>10</sup> D. M. Pozar, *Microwave Engineering*, 4th ed. (John Wiley & Sons, 2011).
  - <sup>11</sup> R. W. Boyd, *Nonlinear Optics*, 2nd ed. (Academic Press, 2003).
  - <sup>12</sup> D. Zhuang, Q. Na, Q. Xie, N. Zhang, L. Zhang, X. Li, G. Zuo, H. Zhang, L. Wang, L. Qin, and J. Song, *IEEE Photonics Journal* **16**, 1 (2024).
  - <sup>13</sup> R. Ding, Y. Liu, Y. Ma, Y. Yang, Q. Li, A. E.-J. Lim, G.-Q. Lo, K. Bergman, T. Baehr-Jones, and M. Hochberg, *Journal of Lightwave Technology* **32**, 2240 (2014).
  - <sup>14</sup> X. Wang, W. Shen, W. Li, Y. Liu, Y. Yao, J. Du, Q. Song, and K. Xu, *Photonics Research* **9**, 535 (2021).
  - <sup>15</sup> P. Kharel, C. Reimer, K. Luke, L. He, and M. Zhang, *Optica* **8**, 357 (2021).
  - <sup>16</sup> Z. Wang, G. Chen, Z. Ruan, R. Gan, P. Huang, Z. Zheng, L. Lu, J. Li, C. Guo, K. Chen, and L. Liu, *ACS Photonics* **9**, 2668 (2022).
  - <sup>17</sup> F. Valdez, V. Mere, and S. Mookherjea, *Optica* **10**, 578 (2023).
  - <sup>18</sup> Y. Du, X. Zou, F. Zou, W. Pan, L. Yan, Q. Zhao, and N. Liu, *Laser & Photonics Reviews*, 2400787 (2024).
  - <sup>19</sup> Y. Zhang, J. Yang, Z. Chen, H. Feng, S. Zhu, K.-M. Shum, C. H. Chan, and C. Wang, *arXiv preprint arXiv:2406.19620* (2024).
  - <sup>20</sup> K. Zhu, V. Saxena, X. Wu, and W. Kuang, *IEEE Transactions on Circuits and Systems II: Express Briefs* **62**, 412 (2015).
  - <sup>21</sup> S. Lin, S. Moazeni, K. T. Settaluri, and V. Stojanovic, *Journal of Lightwave Technology* **35**, 4766 (2017).
  - <sup>22</sup> D. Ming, Y. Wang, Z. Wang, K. X. Wang, C. Qiu, and M. Tan, *IEEE Transactions on Circuits and Systems I: Regular Papers* **71**, 1819 (2024).
  - <sup>23</sup> H. Bahrami, H. Sepehrian, C. S. Park, L. A. Rusch, and W. Shi, *Journal of Lightwave Technology* **34**, 2812 (2016).
  - <sup>24</sup> Q. Zhang, J. Zhou, and J. Hong, *IEEE Photonics Technology Letters* **31**, 1072 (2019).